Key Points:
- The modified analytic solution (MAS) can be applied to altitudes between 0 and 20 km
- The MAS has been extended to droplets radius up to 100 μm
- The MAS works well when irregular shapes of particles are included

Parameterization of In-Cloud Aerosol Scavenging Due to Atmospheric Ionization: Part 4. Effects of Varying Altitude

Liang Zhang[1,3,4] ![ID], Brian Tinsley[2] ![ID], and Limin Zhou[1,3] ![ID]

[1]Key Laboratory of Geographic Information Science, East China Normal University, Shanghai, China, [2]Physics Department, University of Texas at Dallas, Richardson, TX, USA, [3]State Key Laboratory of Numerical Modeling for Atmospheric Sciences and Geophysical Fluid Dynamics, Beijing, China, [4]Institute of Eco-Chongming, East China Normal University, Shanghai, China

Abstract We have verified that the modified analytic solution (MAS) for aerosol scavenging designed in our previous work to parameterize in-cloud collision rate coefficients between aerosol particles and droplets can be extended to altitudes ranging from 0 to 20.6 km, and droplet radii up to 100 μm. The MAS deals separately with the short-range effects and long-range effects involved in the collisions, with the short-range effects including image electric forces, the intercept effect, and the weight effect; and the long-range effects including Brownian diffusion, the Coulomb electric force, and phoretic forces. The effects of Brownian diffusion and Coulomb electric force increase as height increases, while the change of phoretic forces with altitude is complicated. The effects of image electric force and intercept change slightly with altitude, while the weight effect increases significantly at higher altitudes. When the short-range effects include the irregular shape of particles, the MAS also works well. The calculations of collision rate coefficients by our Monte Carlo trajectory model for varying droplet radius, droplet charges, particle radius, particle charges, particle density, relative humidity, pressure and temperature have now been completed, and we parameterize them by the simple MAS method which makes the results user friendly and easily applicable for cloud models. Based on our results, it is now possible to build cloud models to investigate the hypothesized link between the downward current flow in the global electric circuit current and cloud microphysical changes affecting cloud development.

1. Introduction

1.1. Link Between Global Atmospheric Electric Current and Cloud Microphysics

Cosmic rays create ion pairs throughout the atmosphere; outside clouds some of the charges quickly attach to aerosol particles, and inside clouds to droplets as well. So there are always electric charges on particles and droplets in clouds. For the aerosol particles of interest in this work, essentially all collisions with droplets result in sticking, so the collection rate is the same as the collision rate (Pruppacher & Klett, 1997, section 11.5). There are two main categories, defined by droplet size and particle size, for which electric charges modify the net rate of collection (scavenging). The two categories of atmospheric electrical effects on clouds (electro-scavenging and electro-anti-scavenging), where they apply, are capable of affecting cloud albedo, cloud opacity, cloud cover, ice nucleation, and storm invigoration for later stages of cloud development through processes described by Twomey (1977); Rosenfeld et al. (2006, 2008); Tinsley (2012) as we discuss below.

The first category involves image charge attraction, that is, the attraction between a charged aerosol particle and the charge it induces, of opposite sign, on the droplet; a very short range effect that is important for larger particles (micron size) encountering larger droplets. This is because collision rates due to Brownian diffusion are small for larger particles, and the image forces depend strongly on the (roughly inverse cube) distance between particle *surface* and droplet *surface,* which tends to zero before collision. By contrast, the Coulomb electric forces depend on the (inverse square) distance between particle and droplet centers, limited by the sum of droplet and particle radii. Thus a direct effect of electric charges in clouds is to increase the rate of collisions (scavenging) of larger particles. The most important effect is on largely hydrophobic interstitial ice nucleating particles, not removed by nucleation scavenging, nor by phoretic scavenging in updrafts because of the positive supersaturation (Young, 1993). The collection of ice nuclei by image charge attraction in clouds introduces immersion ice nuclei into droplets below the freezing level and causes contact ice

nucleation, in addition to the actual immersion nucleation, above that level, with a consequent increase in total ice production (Tinsley, 2008). We designate this category "electro-scavenging."

The second category involves the effect of Coulomb forces on collision rates for smaller (submicron) particles with droplets, for which image forces do not predominate and collisions rates due to particle diffusion are high. In electrically neutral environments, such as cloud interiors, where droplets and particles each have equal amounts of positive and negative charges, the increase in collision rate between oppositely charged bodies is cancelled, to the first order, by the decrease in collision rates for same-sign charged bodies. This is treated for particle-particle collisions in Pruppacher and Klett (1997, section 18.2). However, at the upper boundaries of stratus-type clouds, there is an accumulation of net positive charge (positive space charge) and at lower boundaries there is an accumulation of net negative charge (negative space charge). In both cases the null effect no longer applies, and there are net decreases in scavenging rate due to the preponderance of repulsive forces.

The space charge appears because of current flow throughout the weakly conducting atmosphere, which constitutes the global atmospheric electric circuit. The current density and space charge vary on day-to-day, decadal, and century time scales. The ionosphere is charged to about 250 kV by thunderstorms, and this potential varies both with thunderstorm variations and with inputs from the solar wind (Frederick & Tinsley, 2018). The downward current density (Jz) of a few pA/m^2, varies with the ionospheric potential and also with the local column resistance of the atmosphere that is caused by variations in the cosmic ray flux; solar and magnetospheric energetic particles; aerosols in the troposphere and in the stratosphere following volcanic eruptions (Hays & Roble, 1979; Tinsley & Zhou, 2006; Williams, 2005).

The space charge at the upper and lower boundaries of stratus-type clouds is created by the current density Jz flowing through the gradients of conductivity. The conductivity inside clouds is a factor of 3–40 less than that outside the clouds at the same altitude (Pruppacher & Klett, 1997, section 18.3.2) owing to the attachment of both positive and negative air ions to droplets, and this reduced conductivity necessitates an increased electric field to maintain current flow through the cloud (Ohm's Law). The increasing magnitude of the downward electric field going into the cloud requires positive excess charge at cloud top; the decreasing magnitude at cloud base requires net negative net charge (Poissons equation). Zhou and Tinsley (2007, 2012) have built a layer cloud model to estimate the production of space charge and its partition between droplets, aerosol particles, and air ions. Many measurements of space charge at the boundaries of stratus-type clouds have been made (Pruppacher & Klett, 1997, section 18.4; Beard et al., 2004; Nicoll & Harrison, 2016).

So the space charge at the boundaries of stratus-type clouds can decrease the rate of scavenging by particle diffusion, which for small condensation nuclei determines a lifetime of less than about an hour (Pruppacher & Klett, 1997, section 17.4.2.1). So over periods of many hours, the cumulative effect is to tend to maintain the population of the smallest particles. We call this process electro-anti-scavenging.

Tropospheric clouds in polar regions appear to be susceptible to electro-anti-scavenging. These clouds consist of one or more stratus layers formed in the clean polar air with quite low concentrations of aerosols and cloud condensation nuclei (CCN), often with optical depth less than unity (Mauritsen et al., 2011; Shupe et al., 2013; Stone, 1993; Silber et al., 2018). Mauritsen et al. (2011) showed that the optical thickness of these clouds varies with the CCN concentration. They are in the region subject to downwelling and mixing with upper tropospheric and stratospheric air with high concentrations of ultrafine particles (Humphries et al., 2016), which are too small to act as CCN, so that electro-anti-scavenging would give these particles time to grow by vapor deposition to become CCN. With continuing or later condensation episodes, the changes in CCN concentration could affect cloud opacity. This process may be the reason for observed or inferred links between small changes in the current density J_z and small changes in high-latitude clouds, radiative coupling, and atmospheric dynamics, including those in the Antarctic and Arctic (Burns et al., 2008; Frederick & Tinsley, 2018; Kniveton et al., 2008; Lam et al., 2013, 2014, 2017; Zhou et al., 2017). Also, the correlations with magnetic activity of Arctic and Antarctic cloud opacity analyzed by Frederick (2016, 2017) and Frederick and Tinsley (2018) are correlations with J_z, which changes in those regions with changing auroral current systems (Frank-Kamenetskii et al., 2012). It is important that the same effects on surface pressure and cloud opacity are found whether the Jz variations, on the day-to-day time scale, are produced by thunderstorm activity internal to the atmosphere or by the solar wind external to it (Burns et al., 2008;

Frederick & Tinsley, 2018). These factors point strongly to the effects being caused by electric charges affecting cloud microphysics, as we simulate and parameterize for electro-scavenging and electro-anti-scavenging in this paper.

1.2. Collision Rate Coefficients

We investigate the effect of electrical and other forces on the particle scavenging, by simulation of particle trajectories relative to the falling droplet center. We determine the collision rate coefficient $R_{A,a,Q,q,RH,\rho,h}$ between particles and droplets, with droplet radius A, droplet charge Q, particle radius a, particle charge q, relative humidity RH, and particle density ρ, and altitude h, while the droplet density is the constant value of 1,000 kg/m^3. The collision rate coefficient is the number of collisions per unit time per unit volume per unit concentrations of droplets and particles. Collision rate coefficients are also known as collision kernels (Tinsley, 2010; Zhou et al., 2009). Because essentially all collisions with droplets with particles of the sizes considered here result in attachment, the collision rate is equivalent to the collection rate. A related parameter is the collision efficiency, which does not take into account the fall speed of the droplet, and is defined as the fraction of the particles in the volume swept out by the collector droplet that collide with it (Tinsley, 2010; Tinsley et al., 2006).

In previous work, the collision rate coefficients were parameterized by fitting polynomials, but this method can be low in accuracy and time consuming (Tinsley & Leddon, 2013; Tinsley & Zhou, 2015; Zhang & Tinsley, 2017, 2018). In our recent work, we designed a modified analytic solution (MAS) for the rate coefficients calculated by the Monte Carlo trajectory model at the altitude of about 5 km, with pressure and temperature of 540 hPa and 256.15 K, which deals with the short-range and long-range effects separately (Zhang et al., 2018). In the present work, we will show how well the MAS works, for altitudes ranging from 0 to 20.6 km, by comparing it to with results of simulations for discrete parameter values. The collision rate coefficients $R_{A,a,Q,q,RH,\rho,h}$ are calculated by the Monte Carlo trajectory model, for droplet radii A of 3, 6, 9, 12, 15, 30, 50, 100 μm; droplet charges Q of −100e, −50e, −20e, −10e, 0e, 10e, 20e, 50e, and 100e; particle radius a varying from 0.01 μm to values close to A; particle charge q of 0e, 10e, 20e, 50e; particle densities ρ of 500, 1,000, 1,500, and 2,000 kg/m^3; relative humidities RH of 95%, 98%, 99%, 100%, and 101%.

In section 2, we will introduce the Monte Carlo trajectory model as well as the MAS method in detail. In section 3, we will show the changes of the short-range and long-range effects along with height and verify the ability of the MAS to work well at varying altitudes. A short summary will be given in section 4.

2. Theory and Methods

2.1. The Monte Carlo Trajectory Model

The Monte Carlo trajectory model is given in the Appendix A. Our Monte Carlo trajectory model has continually evolved and now includes effects of intercept, weight, inertia, flow around the particle, phoretic forces, electric forces, and diffusion (Tinsley, 2010; Tinsley et al., 2000, 2006; Tinsley & Leddon, 2013; Tinsley & Zhou, 2015; Zhang & Tinsley, 2017, 2018).

The electric forces include image electric forces as well as the Coulomb force and are as given by Davis (1964a, 1964b) and Khain et al. (2004). The droplets and particles are treated as two conducting spheres, with the larger sphere as the droplet and the smaller as the particle. (Zhou et al., 2009). There is an image force between the charge on the particle and the image charge of opposite sign that it induces on the conducting droplet. There is also an image force between the charge on the droplet and the image charge it induces on (larger) particles. The image forces are always attractive, which generates the electro-scavenging effect; the Coulomb force is repulsive when the sign of charges on the droplet and the particle are same, which generates the electro-anti-scavenging effect.

It should be noted that in the regions with temperature below about −40 °C, most of the supercooled droplets will be frozen into ice crystals existing in the habits such as planar, columnar, and broad-branch, the Reynolds numbers for which range from 0.1 to about 100. The collision efficiencies for ice crystals scavenging the aerosol particles or supercooled droplets are both significantly influenced by the Reynolds numbers and thus by the shape of ice crystals (Feng, 2009; Wang & Ji, 2000). In our Monte Carlo trajectory model, the flow field around the droplets are obtained on the assumption of spherical droplet and low Reynolds number (Tinsley et al., 2006), so that our results could not be applied to the ice crystals of large Reynolds number.

Table 1
Pressures, Temperatures, and Altitudes Used in Simulations

P (hPa)	T(°C)	T(K)	Approx. Alt. (km)
50	−56	217.15	20.6
100	−56	217.15	16.2
140	−56	217.15	14.0
180	−56	217.15	12.5
300	−45	228.15	9.2
540	−17	256.15	5.0
700	−5	268.15	3.0
850	5	278.15	1.5
1013	15	288.15	0.0

2.2. Review of MAS

When only purely inverse-square forces are considered, namely, Coulomb and phoretic forces, in association with Brownian diffusion, there exists an analytic solution of collision rate coefficients in flux model, as given by the equation (B5) in Appendix B. However, this analytic solution is not applicable when short-range effects are included, such as intercept effect, image electric forces, weight effect, inertia, and the flow around particle effect, which are described by Zhang et al. (2018, Table 1). The MAS method is designed by modifying the analytic solution to make it take account of the short-range effects Zhang et al. (2018, section 3.1).

The short-range effects generally become very strong when particles move close to the droplet surface and quickly decrease to zero when particles move far away. Thus, there should exist a distance between particles and the droplet, less than which particles would be captured by the droplet and larger than which the short-range effect can be ignored. We call such a distance as effective collision radius (ECR) and use A' to indicate it. When the distance between the particle and the droplet is greater than A' short-range effects disappear and only purely inverse-square forces are present, in which case the analytic solution of rate coefficient given by equation (B5) works. The MAS modifies the analytic solution by substituting A' for the droplet radius A and uses y to indicate the ratio, that is, $y = A'/A$, and then the collision rate coefficient in MAS is given by the following expression

$$R = N_B \frac{x}{e^{x/y} - 1}, \tag{1}$$

where R is the collision rate coefficient, N_B is Brownian diffusion rate coefficient, x is the sum of x_e and x_p, which are used to measure the Coulomb force and phoretic force, respectively. The parameter y is the ratio between ECR and droplet radius, when y is equal to 1, there is no short-range effect, and equation (1) reduces to the analytic solution; when y is larger than 1, the rate coefficients increase because the short-range effects make collision easier to occur.

For simplicity in dealing with the particle size range, in this paper "small particles" refers to particles with radii less than 0.2 μm, and "large particles" refers to particles with radii larger than 0.2 μm. For small particles, the short-range effect is mainly determined by the image charge induced by particles, and the long-range effect is mainly determined by the Coulomb electric force. For larger particles, the short-range effect also includes intercept, weight, and inertial effects, in conjunction with the image charges induced by droplets, and the long-range effect is often dominated by phoretic forces. We parameterize the y value in equation (1) for the two ranges separately.

For small particles the short-range effect only includes the image charges induced by particle charges. Zhang et al. (2018) searched a variety of functional forms and found the following y value fitting the simulations well

$$y_{a<0.2\mu m} = \begin{cases} 1 + e^{-x/(4+4z)}(z-1), & \text{for } x>0 \\ 1 + \left(1 - \dfrac{x}{4+4z}\right)(z-1), & \text{for } x\leq 0 \end{cases}, \tag{2}$$

where z reflects the effect of image charge and is given by

$$z = \frac{R_{A,a,0,q,100\%,500,h}}{N_B}. \tag{3}$$

When the effect of image charge is negligible, the z in equation (3) approaches 1, and then the y value in equation (2) will be equal to 1, which means the effective collision radius reduces to the droplet radius.

For large particles the short-range effects include the intercept effect, the weight effect, and image electric forces induced by particles charges as well as by droplet charges. Zhang et al. (2018) gave the y value as
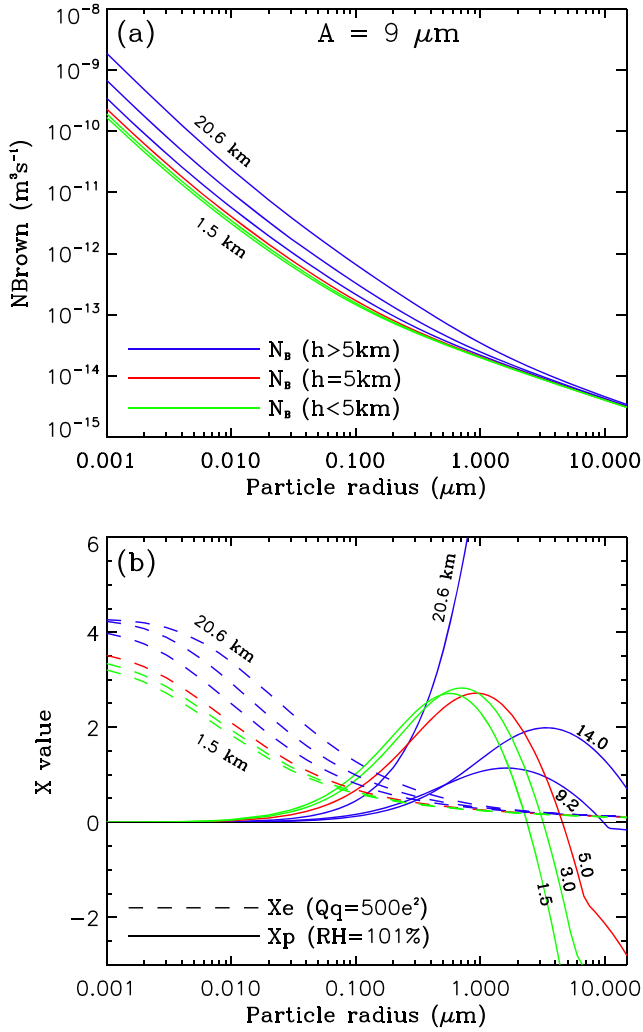
Figure 1. Variation with altitude of collision rates due to Brownian motion and x values: (a) Brownian collision rate coefficient N_B for 9-μm droplet; (b) The x values for a 9-μm droplet, with solid lines representing the x_p value for phoretic forces of $RH = 101\%$, and dashed lines representing the x_e value for Coulomb electric forces of $Qq = 500e^2$. The green, red, and blue lines correspond for the results at 1.5 and 3.0 km levels, at 5 km level, and at 9.2, 14.0, and 20.6 km levels, respectively.

$$y_{a\geq 0.2\mu m} = 1 + y_1 + y_2 + y_3, \tag{4}$$

and the y_1, y_2, and y_3 are obtained with the similar functional form as equations (2) and (3). y_1 mainly includes the intercept effect, as well as the weight effect, inertia effect, and the effect of flow around the particle

$$y_1 = \begin{cases} e^{\frac{x}{10+15u}}(u-1), \text{for } x>0 \\ \left(1-\frac{x}{10+15u}\right)(u-1), \text{for } x\leq 0 \end{cases}, \tag{5}$$

where

$$u = \frac{R_{A,a,0,0,100\%,\rho,h}}{N_B} \tag{6}$$

and y_2 represents the effect of the image electric force induced by the particle charge,

$$y_2 = \begin{cases} e^{\frac{x}{5+8u}}v, \text{for } x>0 \\ \left(1-\frac{x}{5+8u}\right)v, \text{for } x\leq 0 \end{cases}, \tag{7}$$

where

$$v = \frac{R_{A,a,0,q,100\%,\rho,h}-R_{A,a,0,0,100\%,\rho,h}}{N_B} \tag{8}$$

and y_3 includes the effect of the image electric force induced by droplet charge,

$$y_3 = \begin{cases} e^{\frac{x}{3+4u}}w, \text{for } x>0 \\ \left(1-\frac{x}{3+4u}\right)w, \text{for } x\leq 0 \end{cases} \tag{9}$$

where

$$w = \frac{R_{A,a,Q,0,100\%,\rho,h}-R_{A,a,0,0,100\%,\rho,h}}{N_B}. \tag{10}$$

The effect of the image electric force induced by the droplet charge usually is weak and only exists when the size of the droplet and particle are comparable, thus most of the time it can be ignored (Zhang & Tinsley, 2017, 2018).

When the particle is heavy enough the collision rate coefficient can be less than the Brownian rate, that is, $R_{A,a,0,0,100\%,\rho,h} < N_B$, the definition of ECR is no longer valid and the MAS does not hold. For this condition, Zhang et al. (2018) suggested an alternative formula to fit the rate coefficients, provided the value of x is small,

$$R_{A,a,Q,q,RH,\rho,h} = R_{A,a,0,0,100\%,\rho,h}\frac{x}{e^x-1}, \text{for } R_{A,a,0,0,100\%,\rho,h}<N_B. \tag{11}$$

Zhang et al. (2018) has verified the above formulas works well for mid-tropospheric (~5 km) conditions (540 hPa, 256.15 K) for droplet radius up to 15 μm. For the present work we selected nine levels with altitudes ranging from 0 to 20.6 km, with pressures and temperatures given by the U.S. Standard Atmosphere (COESA, 1976) for midlatitudes, as shown in Table 1. In the next section, we will show changes of short-range and long-range effects and check the performance of the MAS for these altitudes.
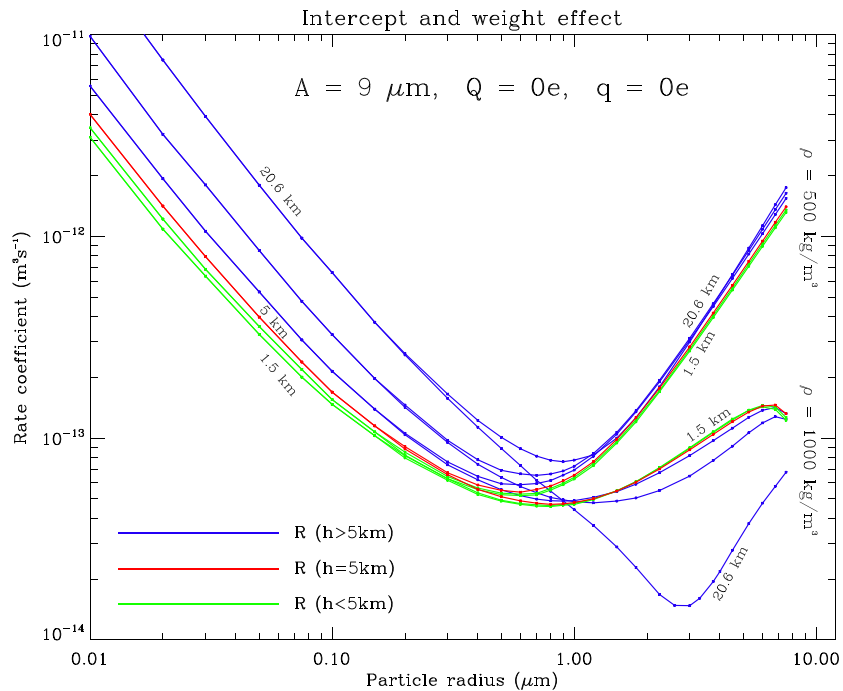
Figure 2. Variation with altitude of collision rates due to particle intercept and weight: the collision rate coefficients for a droplet radius of 9 μm with particle densities of 500 kg/m^3 and 1,000 kg/m^3 which illustrate the intercept effect and weight effect, respectively. The green, red, and blue lines correspond for the results at 1.5 and 3.0 km levels, at 5 km level, and at 9.2, 14.0, and 20.6 km levels, respectively.

3. Results

3.1. The Changes of Long-Range Effects With Altitude

The Brownian diffusion, the Coulomb electric force, and the phoretic forces are long-range influences, measured by the N_B, x_e, and x_p values. As shown in Figure 1a, the N_B value for a 9-μm droplet increases as the height increases, because the atmospheric density reduces and the mean free path of the random motion of the particles increases with the increasing altitude. The N_B value changes are more significant for smaller particles. Figure 1b shows the values of x_e and x_p for a 9-μm droplet, the x_e value simply increase with altitude, while the x_p value changes in a complicated way. The phoretic forces consist of thermophoretic force and diffusiophoretic force, so that the x_p value is the sum of the corresponding x_{Th} and x_{Df} value. The direction of the thermophoretic force and the diffusiophoretic force are opposite, and they vary with particle radius; there generally exists a crossover point where the x_p value will change sign. The change in sign of the x_p value is at a particle radius of about 4.5 μm for the 5.0-km level and it decreases to about 2.0 μm at the surface sea level. The crossover point increases to a large value at altitudes higher than 9.2 km, with x_p remaining positive. In order to be easily used, the values of N_B, x_e, and x_p have been parameterized at the 5-km level and were listed in the Appendix of Zhang et al. (2018).

3.2. The Changes of Short-Range Effects Over Altitudes

Figure 2 shows the collision rate coefficients for droplet radius of 9 μm, with altitudes varying from 0 to 20.6 km. For larger particles the results for those of density of 500 kg/m^3 are dominated by the intercept effect, and those of 1,000 kg/m^3 are dominated by the weight effect. The intercept and weight effect are both negligible for small particles at all heights. The intercept effect changes slightly with altitude, while the weight effect makes the collision rate coefficients decrease significantly for altitudes higher than 5 km. There, the rapidly decreasing pressure would result in smaller drag, if other things remained equal. With the constant gravitational force the trajectory moves further outwards when below the droplet and the probability of a collision is reduced. The values of $R_{A,a,0,0,100 \%,500,h}$ for altitudes less than 5 km are same as those of 5 km, and the vales for altitudes of 5, 9.2, 12.5, and 14 km are given in the Appendix C1.
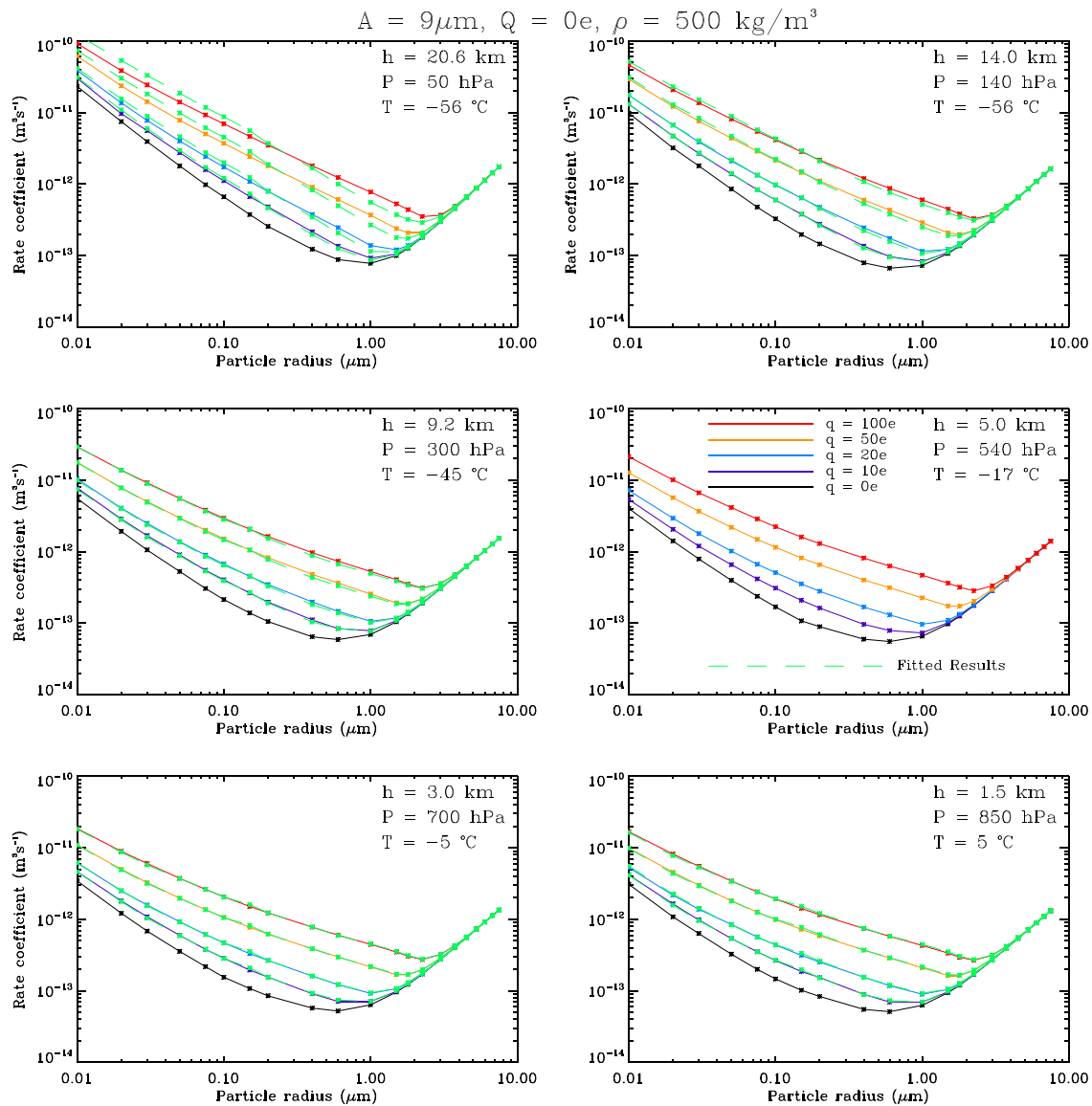
Figure 3. Variation with altitude of collision rates due to the image electric force, with droplet radius of 9 μm, droplet charge of 0e, particle charge of 0e, 10e, 20e, 50e, 100e, particle density of 500 kg/m^3, and with altitudes varying from 1.5 to 20.6 km. The green dashed lines are the fitted results by equation (12).

Figure 3 shows the collision rate coefficients including the effect of image electric force induced by particle charge, with droplet radius of 9 μm, droplet charge of 0e, particle charges of 10e, 20e, 50e, 100e, particle density of 500 kg/m^3, and altitudes varying between 1.5 and 20.6 km. The image electric force will result in electro-scavenging effect, which is obvious for each altitude, as shown in Figure 3. For particles with radius greater than about 3.0 μm, the intercept effect overcomes that of the image electric force at all altitudes. The relative increment of collision rate coefficients caused by image electric force can be roughly viewed as constant over varying heights, Zhang et al. (2018) obtained the results of 500 kg/m^3 at the height of 5 km, based on which we can get the collision rate coefficient including the image electric force at the height of h

$$R_{A,a,0,q,100\%,500,h} \approx \frac{R_{A,a,0,0,100\%,500,h}}{R_{A,a,0,0,100\%,500,5km}} R_{A,a,0,q,100\%,500,5km}. \tag{12}$$

The green dashed lines in Figure 3 represents the results of equation (12), which match well with the results calculated by our Monte Carlo trajectory model for altitudes lower than 14 km. In this and the following

Figure 4. Effects of droplet radius at 14 km: the comparison between the calculated results of collision rate coefficient (solid lines) and the fitted results by equations (1), (2), and (3) (dashed green lines), with droplet charges varying from −100e to 100e, droplet radius varying from 3 to 100 μm, particle charge of 10e, and relative humidity of 99%, at the altitude of 14 km, temperature of −56 °C, pressure of 140 hPa.

figures, "match well" means the average errors are less than 10%. Besides, the increment of collision rate coefficient caused by image electric forces changes little for particle density, thus the rate coefficient for particle density other than 500 kg/m^3 can be obtained by

$$R_{A,a,0,q,100\%,\rho,h} \approx R_{A,a,0,0,100\%,\rho,h} + \left(R_{A,a,0,q,100\%,500,h} - R_{A,a,0,0,100\%,500,h} \right). \tag{13}$$

The values of $R_{A,a,0,q,100\%,500,5km}$ for particle charges of 10e, 20e, 50e, and 100e are given in the Appendix *C2*.

The effect of the image electric force induced by droplet charge can also enhance the collision rate coefficients between small droplets and large particles, and there also exist relations similar to equations (12) and (13) but for a change of "*0,q*" to "*Q,0*." This effect is negligible when the droplet radius is larger than
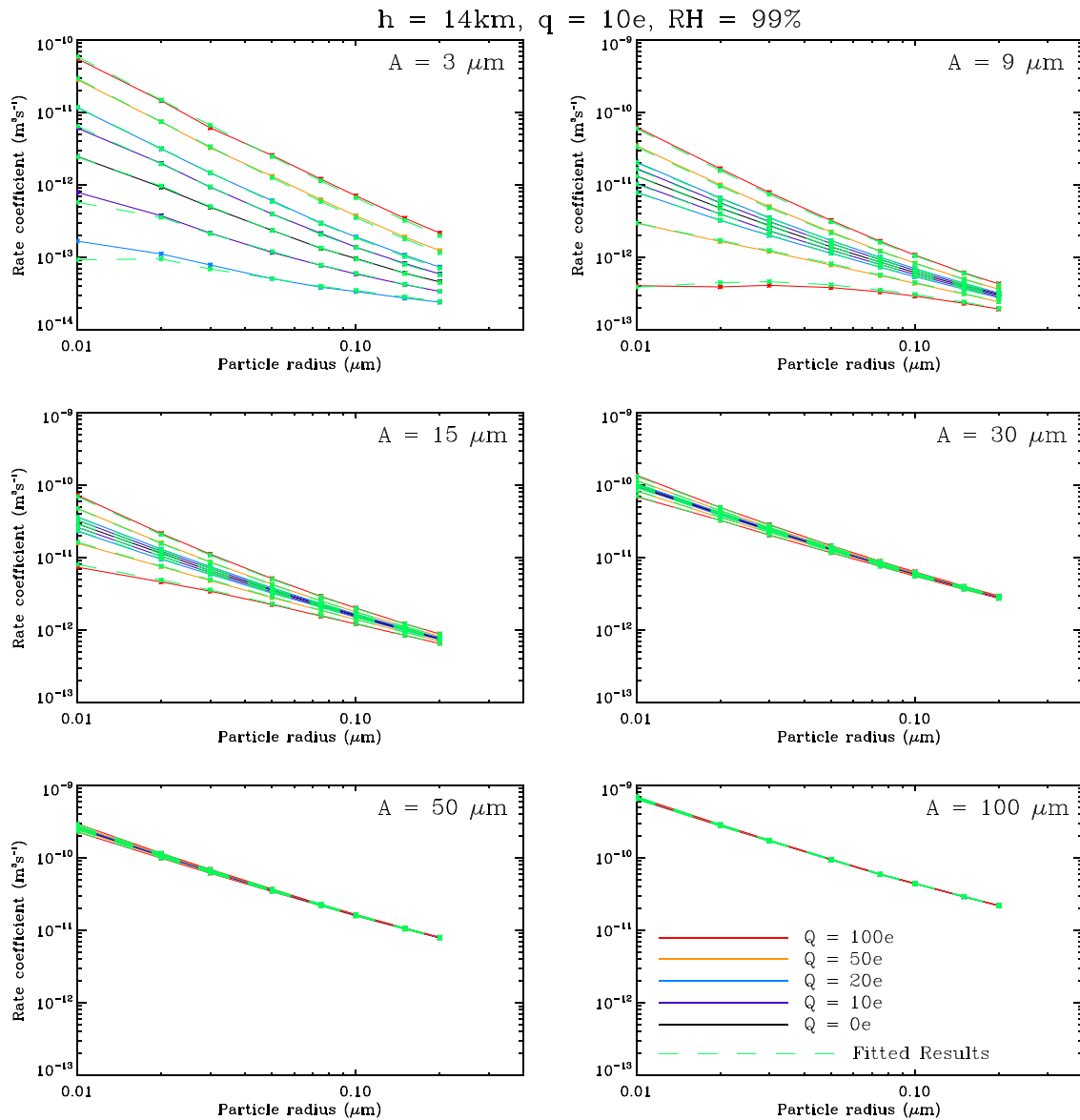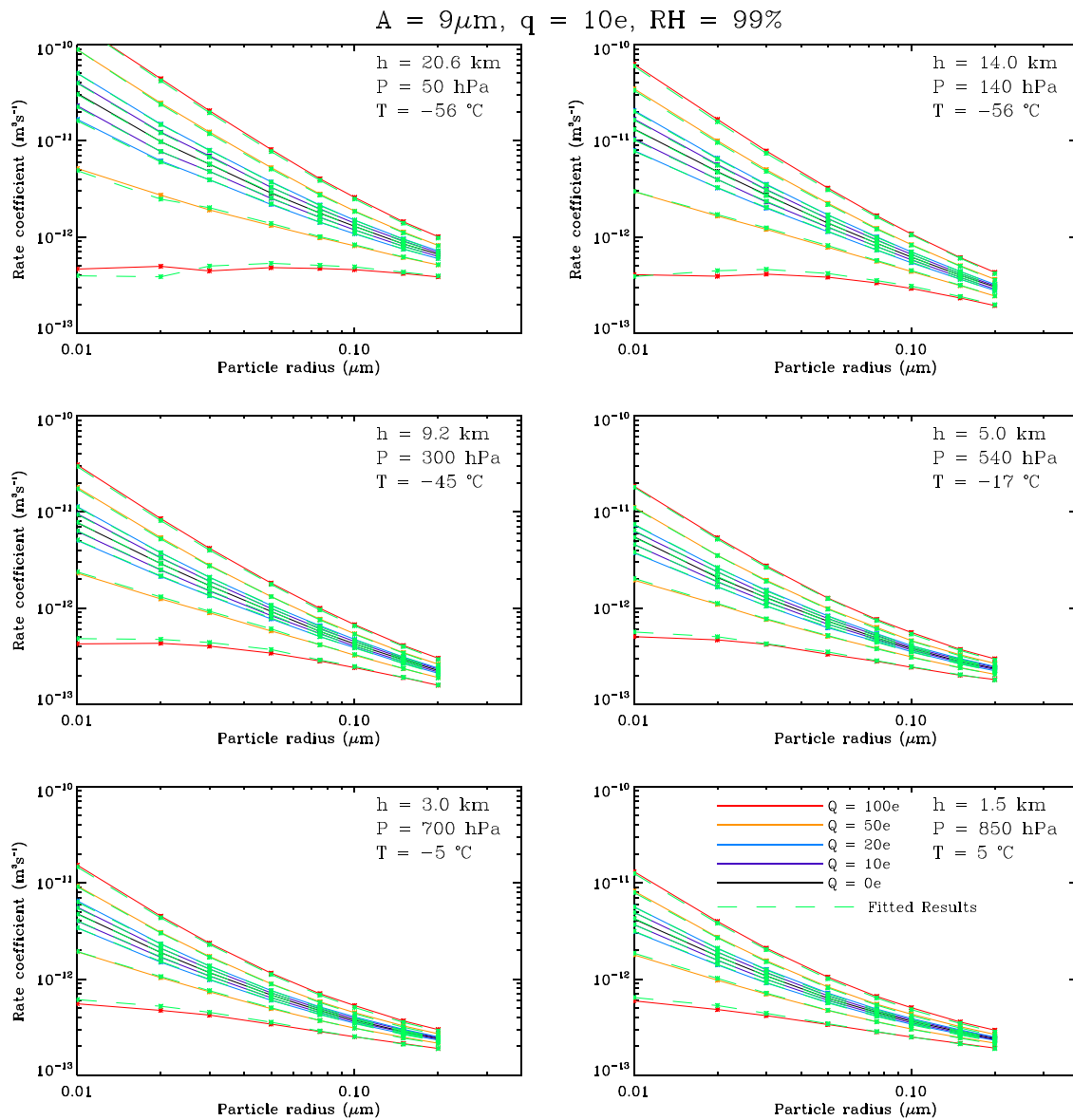
Figure 5. Variation with altitude of the effects of droplet charge: comparison between the calculated results of collision rate coefficient (solid lines) and the fitted results by equations (1) and (2) (dashed green lines), with droplet charges varying from −100e to 100e, droplet radius of 9 μm, particle charge of 10e, relative humidity of 99%, and altitudes varying from 1.5 to 20.6 km.

6 μm or the particle radius is less than 0.2 μm. The values of $R_{A,a,Q,0,100\ \%\ ,1000,5\ km}$ for particle charges of 10e, 20e, 50e, and 100e are given in the Appendix C3.

The results in Figures 2 and 3 are similar for other droplet radii, not shown. Generally speaking, the intercept effect and the effect of image electric force change little with altitude, because they take effect within a very narrow region around the droplet, and this is not strongly affected by altitude. However, the relative particle and droplet trajectory is determined by air drag, which becomes significant as the air density rapidly decreases with altitude. Later we will show that this will influence the performance of the MAS.

3.3. Comparison of MAS With Simulations for Varying Altitude
3.3.1. The MAS for Small Particles ($a < 0.2$ μm)
In our previous work, we have shown that the results of the MAS match well with the results of Monte Carlo trajectory model for small particles, with droplet radius ranging between 3 and 12 μm, altitude at 5 km
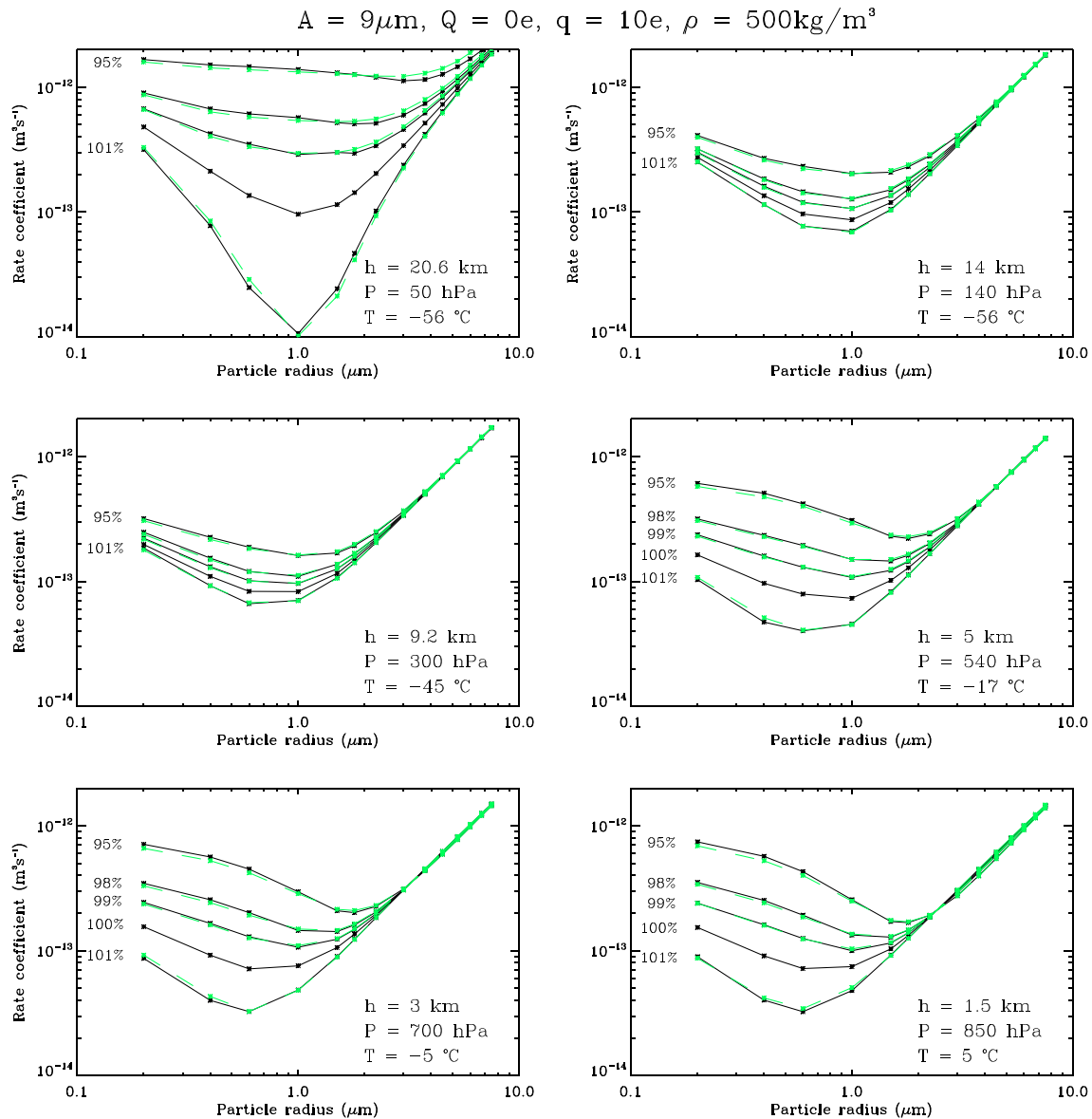
Figure 6. Variation with altitude of the effects of relative humidity: the calculated results (solid black lines) of the Monte Carlo trajectory model and the fitted results by equations (1) and (4) (green dashed lines), for droplet charge of 0e, particle charge of 10e, particle density of 500 kg/m^3, *RH* of 95%, 98%, 99%, 100%, and 101%, and altitude varying from 1.5 to 20.6 km.

(Zhang et al., 2018, Figure 3). In Figure 4, the altitude is moved up to 14 km, droplet radii are extended to 100 μm, and again we compare the simulated results of rate coefficients $R_{A,a,Q,10e,99\ \%\ ,500,14km}$ (solid lines) with the results of MAS (green dashed lines), the droplet charges Q range from −100e to 100e. The short-range effect is only determined by image electric force, thus in MAS method equations (1) and (2) are used to calculate the rate coefficients, and it is obvious that the results of MAS match very well with the simulated results for small particles. In addition, the long-range effects become weaker for larger droplets and can be ignored when the droplet radii are greater than 100 μm, this is because the x_e and x_p value both decrease with increasing droplet radius (Zhang et al., 2018, Figure 1). Figure 5 similarly compares the MAS results and simulated results of a 9-μm droplet collecting small particles, for altitude varying from 1.5 to 20.6 km, and the MAS works well in this range. The x_e value shown in Figure 1 becomes greater as height increases, thus the "width" of the cluster of curves in Figure 5 of higher altitudes is larger than that of lower altitudes. When the droplet and the particle are charged with same
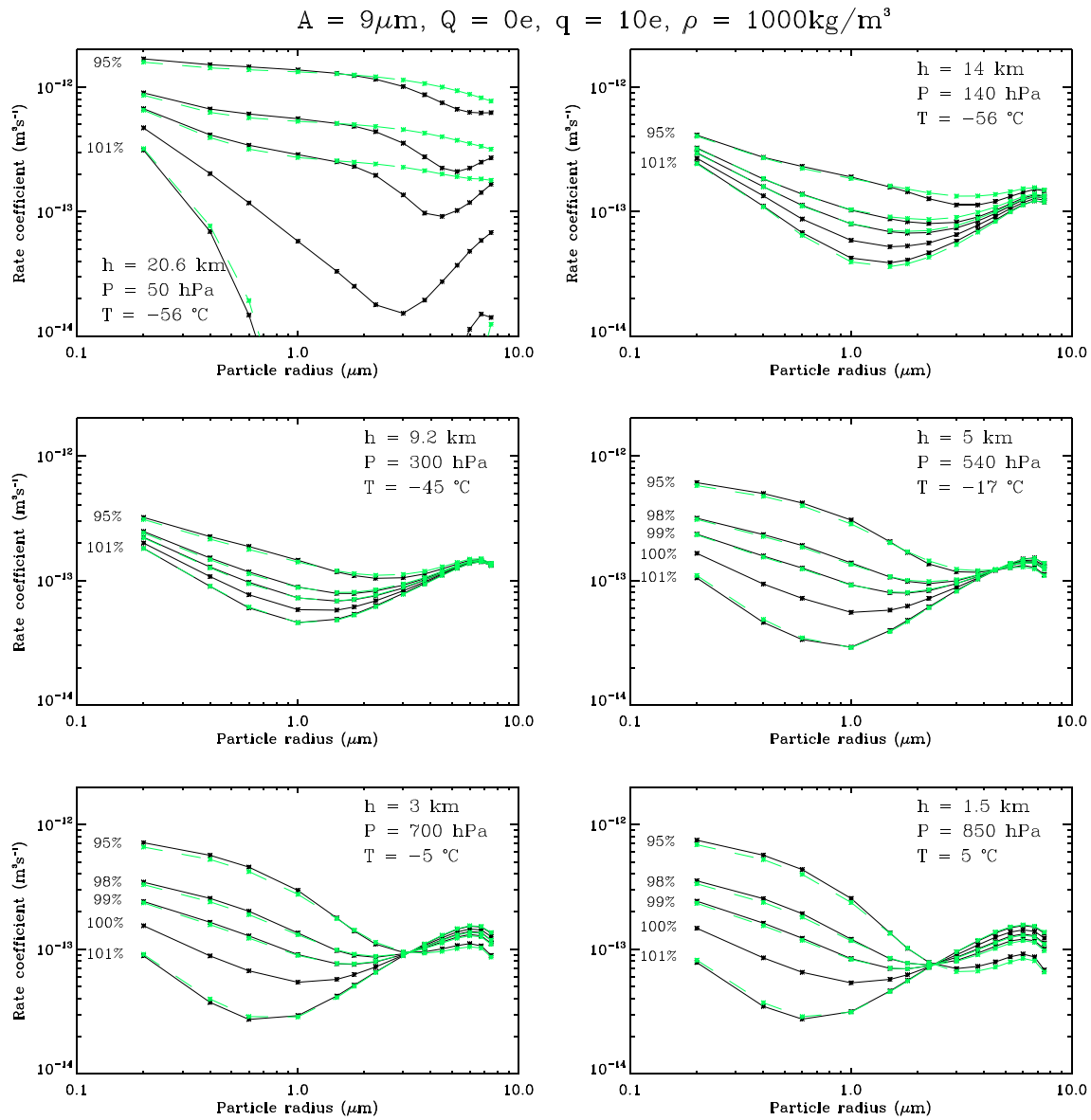
Figure 7. The same as Figure 6 but for particle density of 1,000 kg/m^3.

sign, the repulsive Coulomb force will result in the electro-anti-scavenging effect, which becomes more evident for higher altitudes, as shown in Figures 4 and 5.

3.3.2. The MAS for Large Particles ($a > 0.2$ μm)

For large particles, the short-range effects include image electric force, intercept effect, and weight effect, thus in MAS method equations (1) and (4) are used to calculate the collision rate coefficients in order to including the above short-range effects. Figure 6 compares the MAS results (green dashed lines) with the simulated results (black solid lines) of collision rate coefficients between 9-μm droplet and large particles, with droplet charge of 0e, particle charge of 10e, particle density of 500 kg/m^3, relative humidity of 95%, 98%, 99%, 100%, and 101%, and altitudes varying from 1.5 to 20.6 km. For particles with density of 500 kg/m^3, the intercept effect dominates over weight effect, and in which case the MAS works well. The x_p value in Figure 1 changes in a complicated way with altitude, which is reflected by the width of curve clusters in Figure 6.

Figure 7 is similar to Figure 6, but for the particle density of 1,000 kg/m^3. We can see that the MAS works well from 1.5 to 20.6 km height when particle radius is smaller than 2.0 μm. However, when the particle radius is larger than 2.0 μm, the MAS works well only for altitudes lower than 14 km and is poor for

Figure 8. The same as Figure 6 but for particle density of 1,500 kg/m^3. The red dashed lines represent the results of equation (11) when $R_{A,a,0,0,100\,\%\,,\rho,h} < N_B$. The orange line is N_B, the Brownian rate coefficient.

higher altitudes. As shown in Figure 2, the weight effect changes little at lower altitudes but becomes significant at high altitudes. The weight effect can significantly reduce the agreement of the collision rate coefficients with the MAS above about 14 km, and it fits the simulations poorly, however the MAS can be applied in the troposphere, and would cover the whole altitude range of a deep convective cloud or a layer cloud.

Figures 8 and 9 are similar as Figure 6, but for particle density of 1,500 kg/m^3 and 2,000 kg/m^3, respectively. When the collision rate coefficients $R_{A,a,0,0,100\,\%\,,\rho,h}$ is larger than N_B (yellow lines), we apply the MAS method in equations (1) and (4), as shown by the green dashed lines, again, we can see that the MAS works well. When the collision rate coefficients $R_{A,a,0,0,100\,\%\,,\rho,h}$ is smaller than N_B, the MAS method fails in this condition, and we apply equation (11) to estimate the rate coefficients, as shown by the red dashed lines, and it also works well for relative humidity RH ranging between 99% and 101% for altitudes lower than 14 km, but poor for higher altitudes because the x_p value is too large at these altitudes as shown in Figure 1b.
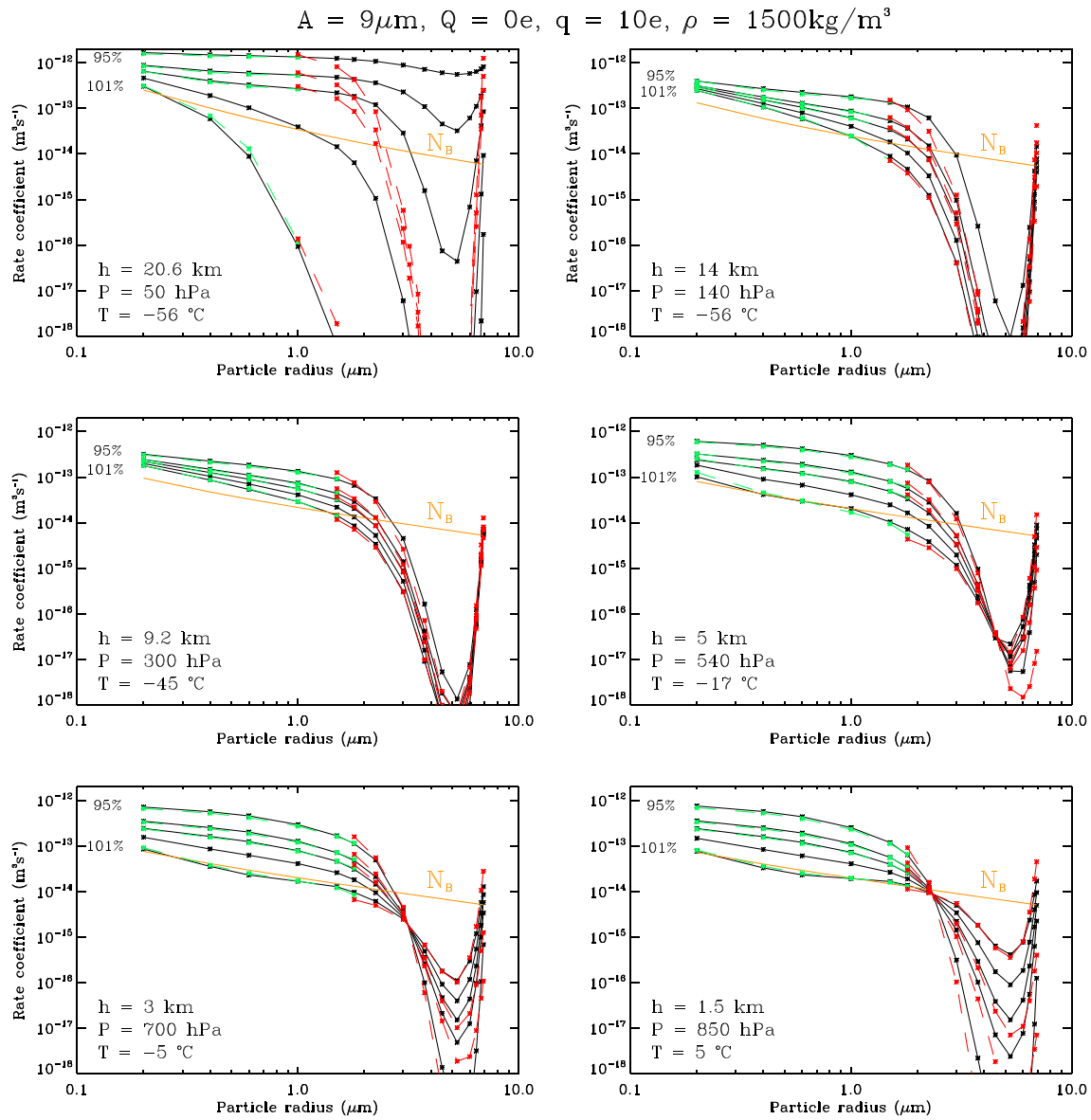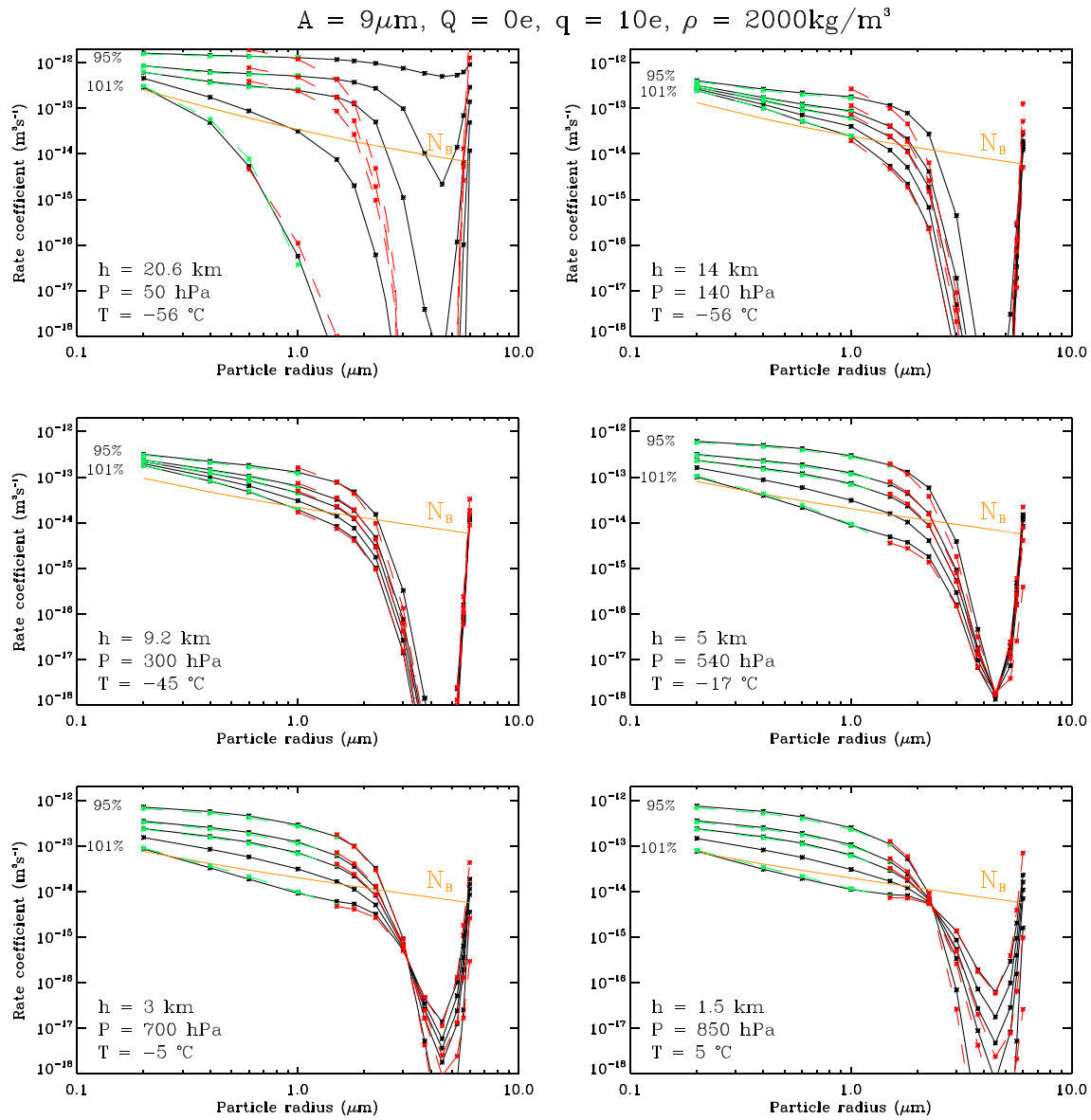
Figure 9. The same as Figure 6 but for particle density of 2,000 kg/m^3. The red dashed lines represent the results of equation (11) when $R_{A,a,0,0,100\%,\rho,h} < N_B$. The orange line is N_B, the Brownian rate coefficient.

Figure 10 is similar to Figure 6, but for the altitude of 14 km, and for droplet radii ranging from 3 to 100 μm. The MAS still works well for varying droplet radii up to 100 μm at 14 km. For particle densities of 1,000, 1,500, and 2,000 kg/m^3, the performance of MAS (not shown) is similar to that in Figures 7, 8, and 9. When the droplet radius is larger than 100 μm, the long-range effect can be ignored as the x value is small for larger droplets. It should be noted that with the large fall speed of large droplets, the inertia of large particles becomes important, which can significantly increase the collision rate coefficients. Also, the effect of image electric forces can be ignored. In short, for droplet radii up to 100 μm, the MAS method can be applied when the particle radius is smaller than 1.0 μm, but when the particle radius is larger than 1.0 μm the short-range inertial effects become predominant.

3.3.3. The MAS in Consideration of the Irregular Shape of Particles

In our Monte Carlo trajectory model, the collisions occur when the distance between droplet center and particle center is exactly equal to the sum of their radii. However, in reality the shape of particles is to some extent irregular with slight deviations from ideal spheres, thus collisions may occur at a distance larger
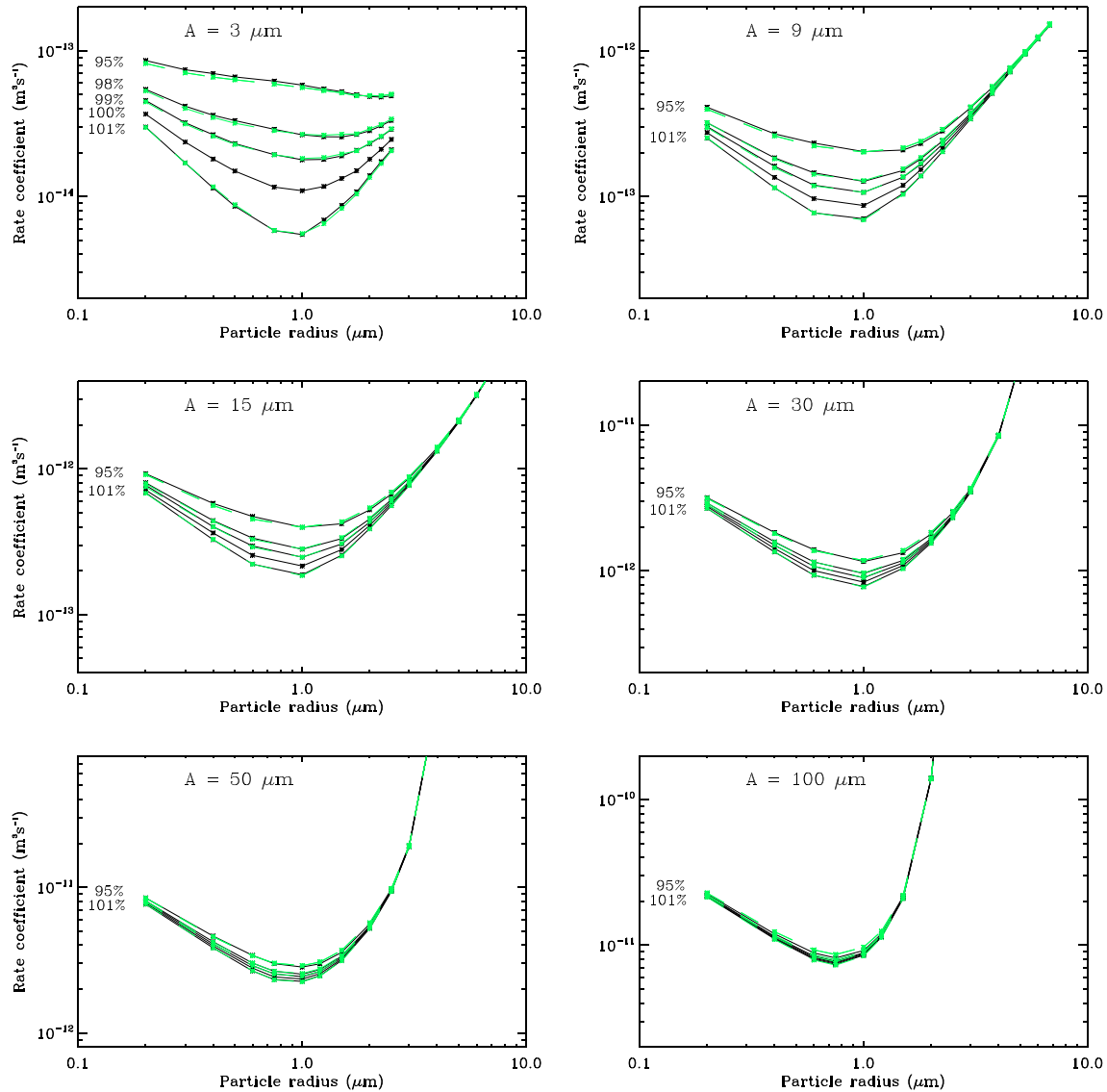
Figure 10. The same as Figure 6, but for altitude of 14 km, and for droplet radii varying from 3 to 100 µm.

than the sum of their average radii. Figure 11 shows the performance of the MAS when varying values of r_c, as an effective collision radius, were set in the Monte Carlo trajectory model, for droplet radius of 9 µm, 14 km in altitude, and particle density of 1,000 kg/m^3. In Figure 11a, the collision radii r_c were set to be 1.0, 1.05, 1.1, and 1.2 ($A+a$), respectively, for droplet charge of 0e, particle charge of 0e. It is obvious that increases in the effective collision radius r_c can significantly increase the rate coefficients. This effect becomes weaker for small particles, which are less affected by short range effects such as intercept effect. Figure 11b is similar to Figure 11a, but the particle is charged with 10e, and in the presence of image electric charges the effect of irregular shape becomes negligible for small particles when r_c is less than 1.10. Figures 11c–11f compare the results of the Monte Carlo trajectory model and the results of MAS, for r_c varying from 1.0 to 1.2(A+a), with droplet charge of 0e, particle charge of 10e, particle density of 1,000 kg/m^3, 14 km in altitude, relative humidity of 95%, 98%, 99%, 100%, and 101%. We treat the irregular shape effect as an increment of the collision radius, in other words, the effect of the irregular shape can increase the collision rate coefficient in a way similar to that of the intercept effect. Meanwhile, the MAS performs very well for the intercept effect as shown in Figures 6 and 10. As expected, Figure 11 clearly shows that the MAS works
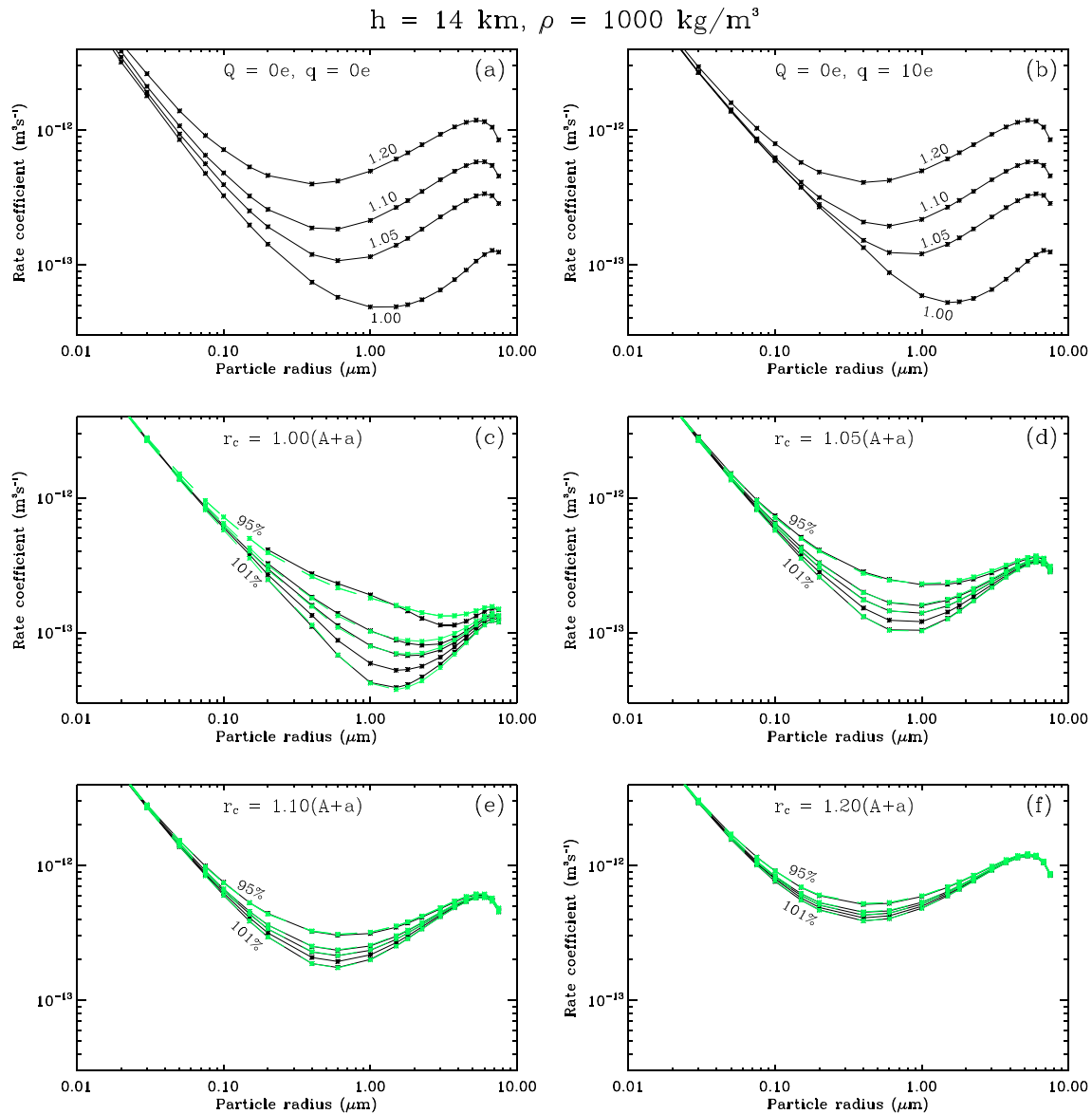
Figure 11. The collision rate coefficients take into account the irregular shape of particles. (a) the $R_{A,q,0,0,100\%,1000,14km}$ for collision radius r_c of 1.0, 1.05, 1.1, and 1.2 ($A+a$), respectively. (b) same as (a) but with particles charged with 10e. (c–f) compare the model results $R_{A,q,0,10,RH,1000,14km}$ and the results of MAS for varying collision radii r_c, with RH of 95%, 98%, 99%, 100%, and 101%, particle density of 1,000 kg/m^3, and 14 km in altitude.

well when the irregular shape is considered. When the weight effect is strong for large particles, the performance of MAS is poorer as shown in Figure 11c as well as Figure 7; while when r_c is larger than 1.05($A+a$), the MAS works well even for large particles as shown in Figures 11d–11f, because the weight effect is offset by the irregular shape effect. Besides, the results for other droplet radii and other altitudes are similar as Figure 11, not shown.

In the regions above 5 km (540 hPa; −17 °C), some supercooled droplets will become ice crystals. If the ice crystals are small and the Reynolds numbers is very low, the flow field around the ice crystal will be similar to that in our Monte Carlo trajectory model, and the density of the droplet can be replaced by the lower density of the ice. Then the collision rate coefficients between aerosol particles and ice crystal can be estimated by our MAS results, with the shape of ice crystal included by adjusting the collision radius r_c. For large ice crystals, the Reynolds numbers will change significantly with the size and shape (Feng, 2009; Wang & Ji, 2000), and the MAS model no longer applies.

4. Summary

We have verified that the MAS used in our previous paper can be applied to varying altitudes from 0 to 20.6 km, applied to droplet radius up to 100 μm, and also applied to the conditions when the irregular shape of particles is considered, with average errors less than 10%. The MAS can be applied to such a wide condition because it is built on the basis of on the assumption of an effective collision radius, which has a solid physical foundation when the short-range effect is dominated by intercept effect or image electric force. The results also show the performance of MAS is poor for large particles with high densities, at altitudes higher than 14 km, but this is above the altitude of most clouds of interest. So now the MAS is suitable for application in cloud models, as we have completed the calculation and parameterization, including the effects of electric charge, for the collision rate coefficients for most cloud microphysical conditions of interest in the troposphere.

Appendix A: The Monte Carlo Trajectory Model

In the Monte Carlo trajectory model, the velocity of an aerosol particle is decided by the following equation

$$m\frac{d\vec{v}}{dt} = \frac{\vec{v}_a - \vec{v}}{B_p} + \vec{f}_e + \vec{f}_p + \vec{f}_g, \tag{A1}$$

where m and $\vec{v}$ is the mass and velocity of the particle; B_p is the mobility of the particle, $\vec{v}_a$ is the velocity of air flow around the droplet, and the term $(\vec{v}_a - \vec{v})/B_p$ is the drag force exerted on the particle. The velocity of air flow is modeled by the Proudman–Pearson expressions for the region adjacent to the droplet, and the Oseen expressions for the region far from the droplet, and a smooth transition between them is used for the intermediate region (Tinsley et al., 2006, section 2). $\vec{f}_e$, $\vec{f}_p$ and $\vec{f}_g$ represent the electric forces, phoretic forces, and gravitational force, respectively. The electric forces include Coulomb force, the image force induced by the droplet, and the image force induced by the particle

$$F_e = \frac{-1}{4\pi\varepsilon_0}\left[Q^2\frac{F_5}{r^2} + Qq\frac{F_6}{r^2} + q^2\frac{F_7}{r^2}\right], \tag{A2}$$

and the values of F_5, F_6, and F_7 can be obtained from lookup tables (Zhou et al., 2009) based on the expressions of Davis (1964a, 1964b). The thermophoretic and diffusiophoretic forces vary with relative humidity and other parameters, and formulas for the variations are given in Appendix A of Tinsley et al. (2006), based on Pruppacher and Klett (1997); see also Davenport and Peters (1978).

The trajectory of the particle can be obtained when the displacement of the particle is calculated during each time step by solving equation (A1) with 4th-order Runge–Kutta method. When the displacement during each time step considers the random motion of the particle, then the diffusion of the particle is included, as described by Tinsley (2010). In the Monte Carlo trajectory model, a large number of particles are released below a falling droplet with radius of A, whose center is treated as the origin of coordinates. Some of the particles, moving upward relative to the droplet, then collide with it, and the probability of collision P_x, as a function of the horizontal offset x of the releasing position from the vertical through the droplet center, is obtained. Then the collision rate coefficient R is calculated by integrating the probability of the range of offsets to the limit of no further collisions, and multiplying by the volume containing falling particles swept out in unit time by the falling droplet

$$R = 2\sum P_x x \Delta x \pi A^2 \left(U_{A,\infty} - u_{a,\infty}\right), \tag{A3}$$

where Δx is the step of the release position, $U_{A,\infty}$ and $u_{a,\infty}$ are the fall speed of the droplet and the particles.

Appendix B: The Analytic Solution of Collision Rate Coefficients in Flux Model

An analytic expression called the "flux mode" has been used by Wang et al. (1978) and Zhou et al. (2009) for electric and phoretic scavenging and is described by Pruppacher and Klett (1997). It is appropriate for use

with the purely inverse square phoretic forces, and for cases where electric forces can be approximated by inverse square forces. The expression used is

$$R = \frac{4\pi B_p C}{\exp\left(B_p C / \left(D_p f_p A\right)\right) - 1},$$ (B1)

where D_p is the particle diffusion coefficient and is related to B_p by the Einstein relation.

$$D_p = kTB_p,$$ (B2)

C is the sum of Coulomb force constant C_e and the phoretic force constant C_p

$$C = C_e + C_p,$$ (B3)

where the Coulomb electric force $F_e = C_e/r^2$ and the phoretic forces $F_p = C_p/r^2$. The phoretic forces include the thermophoretic force and diffusiopheretic force, that is, $C_p = C_{Th} + C_{Df}$ (Tinsley et al., 2006, Appendix). When the forces constant C approaches zero, the rate coefficient R in equation (B1) reduces to $4\pi D_p f_p A$, which is the Brownian diffusion rate coefficient, and is indicated as N_B

$$N_B = 4\pi D_p f_p A.$$ (B4)

Finally, the expression that is equation (B1) can be written as

$$R = N_B \frac{x}{e^x - 1},$$ (B5)

where $x = x_e + x_p$, and

$$x_e = \frac{C_e}{kTf_p A}, x_p = \frac{C_p}{kTf_p A}.$$ (B6)

Appendix C: Results of Rate Coefficient

Table C1
Results of Rate Coefficient $R_{A,a,0,0,100\ \%\ ,\rho,h}$

(h, A, ρ)	0.2 μm	0.4 μm	0.6 μm	1.0 μm	1.5 μm	2.0 μm	2.5 μm	3.0 μm
(5 km, 3, 500)	1.177	0.735	0.668	0.750	1.063	1.482	2.015	—
(5 km, 3, 1,000)	1.157	0.690	0.603	0.547	0.534	0.492	0.380	—
(5 km, 3, 1,500)	1.082	0.643	0.515	0.382	0.248	0.252	—	—
(5 km, 3, 2,000)	1.093	0.636	0.471	0.295	0.301	0.813	—	—
(5 km, 6, 500)	4.153	2.686	2.465	2.928	4.313	6.367	8.923	12.21
(5 km, 6, 1,000)	4.124	2.581	2.218	2.136	2.368	2.703	3.005	3.255
(5 km, 6, 1,500)	4.098	2.433	1.975	1.494	1.032	0.755	0.653	0.582
(5 km, 6, 2,000)	3.971	2.176	1.796	1.124	0.855	0.740	0.642	0.623
(5 km, 9, 500)	9.071	5.842	5.399	6.542	9.833	14.72	20.94	28.42
(5 km, 9, 1,000)	8.870	5.586	4.892	4.788	5.485	6.476	7.607	8.748
(5 km, 9, 1,500)	8.766	5.379	4.373	3.323	2.195	1.140	0.525	0.190
(5 km, 9, 2,000)	8.711	5.187	3.901	2.383	1.386	0.683	0.191	0.027
(5 km, 12, 500)	15.47	10.17	9.317	11.33	16.94	25.52	36.21	48.94
(5 km, 12, 1,000)	15.36	9.649	8.446	8.214	9.197	10.49	11.87	13.21

Table C1 *(continued)*

(h, A, ρ)	0.2 μm	0.4 μm	0.6 μm	1.0 μm	1.5 μm	2.0 μm	2.5 μm	3.0 μm
(5 km, 12, 1,500)	15.13	9.377	7.529	5.583	3.173	0.902	0.062	0.001
(5 km, 12, 2,000)	15.11	8.973	6.684	3.844	1.499	0.190	0.001	0
(5 km, 15, 500)	23.91	15.70	14.68	17.56	26.32	38.98	55.98	75.59
(5 km, 15, 1,000)	23.64	15.13	13.12	12.61	13.78	15.25	16.78	18.48
(5 km, 15, 1,500)	23.37	14.48	11.63	8.334	3.977	0.538	0.008	0
(5 km, 15, 2,000)	23.07	13.87	10.27	5.439	1.125	0.014	0	0
(5 km, 30, 500)	94.78	63.16	58.94	70.92	106.5	159.5	231.1	326.3
(5 km, 30, 1,000)	93.60	60.20	52.32	48.67	50.32	58.61	78.08	146.6
(5 km, 30, 1,500)	92.74	57.59	45.79	28.87	9.521	2.731	2.088	0.670
(5 km, 30, 2,000)	91.61	54.76	39.79	14.10	0.140	0	0	0
(5 km, 50, 500)	246.4	166.5	156.4	195.1	312.7	514.3	857.5	1498
(5 km, 50, 1,000)	244.0	158.4	138.5	135.8	181.3	329.4	849.1	6769
(5 km, 50, 1,500)	244.0	151.3	120.1	81.00	73.64	151.5	6635	3.6e4
(5 km, 50, 2,000)	242.7	143.6	102.5	37.70	11.66	13.05	2.9e4	6.2e4
(5 km, 100, 500)	443.1	328.8	340.2	560.2	1463	6853	16110	41940
(5 km, 100, 1,000)	466.6	321.6	322.0	589.5	7182	3.3e5	6.4e5	8.7e5
(5 km, 100, 1,500)	461.0	313.2	301.9	721.1	2.2e5	6.1e5	8.9e5	1.1e6
(5 km, 100, 2,000)	460.0	305.0	280.5	1315	4.2e5	7.8e5	1.0e6	1.2e6
(9.2 km, 3, 500)	1.377	0.825	0.729	0.808	1.154	1.638	2.238	—
(9.2 km, 3, 1,000)	1.335	0.738	0.643	0.571	0.549	0.508	0.390	—
(9.2 km, 3, 1,500)	1.352	0.730	0.549	0.382	0.258	0.272	—	—
(9.2 km, 3, 2,000)	1.254	0.707	0.500	0.310	0.330	0.974	—	—
(9.2 km, 6, 500)	4.927	2.978	2.663	3.141	4.654	6.919	9.769	13.18
(9.2 km, 6, 1,000)	4.779	2.841	2.351	2.242	2.421	2.718	3.044	3.314
(9.2 km, 6, 1,500)	4.751	2.690	2.098	1.493	0.996	0.739	0.618	0.512
(9.2 km, 6, 2,000)	4.709	2.587	1.865	1.143	0.863	0.700	0.559	0.535
(9.2 km, 9, 500)	10.56	6.458	5.900	6.957	10.47	15.75	22.55	30.59
(9.2 km, 9, 1,000)	10.44	6.211	5.223	4.929	5.433	6.264	7.246	8.194
(9.2 km, 9, 1,500)	10.30	5.899	4.540	3.275	1.915	0.827	0.267	0.050
(9.2 km, 9, 2,000)	10.18	5.571	4.051	2.297	1.210	0.404	0.051	0.002
(9.2 km, 12, 500)	18.33	11.19	10.25	11.99	17.96	27.06	38.45	51.99
(9.2 km, 12, 1,000)	17.92	10.79	9.000	8.318	8.838	9.623	10.49	11.49
(9.2 km, 12, 1,500)	17.88	10.21	7.904	5.337	2.387	0.371	0.004	0
(9.2 km, 12, 2,000)	17.57	9.655	6.845	3.538	0.987	0.032	0	0
(9.2 km, 15, 500)	27.93	17.38	15.88	18.64	27.70	41.04	59.20	80.03
(9.2 km, 15, 1,000)	27.36	16.59	13.97	12.67	13.03	13.59	14.59	15.97
(9.2 km, 15, 1,500)	27.16	15.83	11.61	7.762	2.612	0.103	6.2e-4	0
(9.2 km, 15, 2,000)	27.32	14.89	10.56	4.729	0.486	0	0	0
(9.2 km, 30, 500)	110.0	69.57	63.03	74.26	110.6	166.9	245.2	356.5
(9.2 km, 30, 1,000)	110.1	66.05	54.82	47.61	45.71	53.58	76.64	175.4
(9.2 km, 30, 1,500)	108.7	62.55	46.61	24.66	5.182	0.835	0.504	20.57
(9.2 km, 30, 2,000)	108.5	58.60	39.52	9.401	0.018	0	0	0
(9.2 km, 50, 500)	295.1	189.3	172.7	208.5	331.8	559.0	981.9	1891
(9.2 km, 50, 1,000)	297.3	179.5	149.1	135.3	177.5	359.3	1394	2.0e4
(9.2 km, 50, 1,500)	296.0	168.6	125.9	69.54	56.31	156.6	2.2e4	5.9e4
(9.2 km, 50, 2,000)	292.2	158.3	102.7	24.47	3.718	7018	5.0e4	8.7e4
(9.2 km, 100, 500)	636.8	418.1	417.1	672.6	1916	1.5e4	3.0e5	6.2e5
(9.2 km, 100, 1,000)	626.5	405.5	386.9	735.5	4.5e4	5.2e5	8.8e5	1.2e6
(9.2 km, 100, 1,500)	626.4	391.8	357.6	1068	3.9e5	8.5e5	1.2e6	1.4e6
(9.2 km, 100, 2,000)	623.1	375.9	330.6	6169	6.3e5	1.1e6	1.4e6	1.6e6
(12.5 km, 3, 500)	1.722	0.950	0.749	0.864	1.216	1.740	2.397	—
(12.5 km, 3, 1,000)	1.727	0.888	0.659	0.589	0.556	0.502	0.391	—
(12.5 km, 3, 1,500)	1.649	0.812	0.614	0.395	0.277	0.297	—	—
(12.5 km, 3, 2,000)	1.651	0.778	0.535	0.334	0.360	1.150	—	—
(12.5 km, 6, 500)	5.964	3.354	2.858	3.281	4.812	7.138	10.20	13.80
(12.5 km, 6, 1,000)	5.911	3.149	2.523	2.251	2.345	2.607	2.867	3.121
(12.5 km, 6, 1,500)	5.845	3.028	2.230	1.480	0.952	0.723	0.592	0.492
(12.5 km, 6, 2,000)	5.747	2.861	1.948	1.159	0.882	0.671	0.516	0.467
(12.5 km, 9, 500)	12.69	7.318	6.348	7.214	10.71	16.16	23.12	31.54
(12.5 km, 9, 1,000)	12.63	6.949	5.533	4.914	5.156	5.726	6.432	7.273

Table C1 *(continued)*

(h, A, ρ)	0.2 μm	0.4 μm	0.6 μm	1.0 μm	1.5 μm	2.0 μm	2.5 μm	3.0 μm
(12.5 km, 9, 1,500)	12.38	6.589	4.772	3.139	1.647	0.640	0.151	0.015
(12.5 km, 9, 2,000)	12.55	6.257	4.223	2.285	1.087	0.250	0.016	1.7e-4
(12.5 km, 12, 500)	22.11	12.52	10.98	12.26	17.98	27.12	38.58	52.24
(12.5 km, 12, 1,000)	21.68	11.90	9.450	8.127	7.953	8.065	8.326	8.793
(12.5 km, 12, 1,500)	21.64	11.39	8.190	4.956	1.790	0.161	0.0002	0
(12.5 km, 12, 2,000)	21.41	10.69	7.090	3.281	0.712	0.008	0	0
(12.5 km, 15, 500)	34.01	19.53	16.95	19.06	27.82	41.73	59.28	80.30
(12.5 km, 15, 1,000)	33.22	18.54	14.63	12.27	11.46	11.09	11.38	12.20
(12.5 km, 15, 1,500)	33.39	17.55	12.51	7.067	1.534	0.017	0	0
(12.5 km, 15, 2,000)	32.98	16.47	10.73	4.179	0.243	0	0	0
(12.5 km, 30, 500)	132.3	77.97	67.05	74.52	109.0	164.0	243.4	361.4
(12.5 km, 30, 1,000)	132.3	72.50	56.90	44.76	37.70	42.55	63.11	174.2
(12.5 km, 30, 1,500)	130.6	68.31	47.64	19.72	2.081	0.101	0.023	593.8
(12.5 km, 30, 2,000)	129.2	63.86	38.91	5.852	0.002	0	0	0
(12.5 km, 50, 500)	369.6	214.9	186.7	212.7	328.3	554.0	995.4	2015
(12.5 km, 50, 1,000)	367.2	201.8	157.3	125.4	149.1	314.8	1727	2.7e4
(12.5 km, 50, 1,500)	361.4	187.8	127.8	52.35	28.50	75.24	3.0e4	6.9e4
(12.5 km, 50, 2,000)	357.6	174.4	100.1	12.34	0.363	1.5e4	6.1e4	9.9e4
(12.5 km, 100, 500)	926.8	556.7	517.8	767.9	2130	1.8e4	3.6e5	7.4e5
(12.5 km, 100, 1,000)	918.3	532.3	465.3	791.5	7.0e4	6.4e5	1.1e6	1.4e6
(12.5 km, 100, 1,500)	915.0	508.3	414.6	1138	5.0e5	1.0e6	1.4e6	1.7e6
(12.5 km, 100, 2,000)	905.4	480.2	365.9	2.1e4	7.9e5	1.3e6	1.7e6	1.9e6
(14 km, 3, 500)	1.954	0.997	0.832	0.900	1.235	1.766	2.448	—
(14 km, 3, 1,000)	1.895	0.948	0.705	0.595	0.544	0.488	0.381	—
(14 km, 3, 1,500)	1.858	0.823	0.645	0.395	0.288	0.311	—	—
(14 km, 3, 2,000)	1.894	0.859	0.546	0.356	0.379	0.137	—	—
(14 km, 6, 500)	6.836	3.686	2.996	3.318	4.803	7.157	10.21	13.87
(14 km, 6, 1,000)	6.716	3.450	2.634	2.239	2.246	2.440	2.678	2.917
(14 km, 6, 1,500)	6.586	3.228	2.290	1.472	0.952	0.736	0.583	0.480
(14 km, 6, 2,000)	6.492	3.046	2.011	1.178	0.905	0.667	0.511	0.467
(14 km, 9, 500)	14.53	7.901	6.676	7.262	10.68	16.06	22.97	31.26
(14 km, 9, 1,000)	14.22	7.424	5.736	4.858	4.875	5.273	5.825	6.486
(14 km, 9, 1,500)	13.95	7.016	4.939	3.057	1.553	0.603	0.130	0.011
(14 km, 9, 2,000)	14.09	6.739	4.307	3.057	1.053	0.221	0.012	1.5e-4
(14 km, 12, 500)	24.60	13.51	11.32	12.25	17.70	26.42	37.54	51.00
(14 km, 12, 1,000)	24.31	12.71	9.753	7.837	7.210	6.842	6.809	6.936
(14 km, 12, 1,500)	24.26	12.08	8.321	4.719	1.538	0.134	0.0002	0
(14 km, 12, 2,000)	24.16	11.33	7.229	3.243	0.639	0.005	0	0
(14 km, 15, 500)	37.87	20.95	17.54	18.83	27.06	40.74	57.70	78.60
(14 km, 15, 1,000)	37.62	19.75	15.02	11.90	10.24	9.215	9.098	9.590
(14 km, 15, 1,500)	37.49	18.65	12.80	6.595	1.219	0.006	0	0
(14 km, 15, 2,000)	36.93	17.54	10.88	3.946	0.187	0	0	0
(14 km, 30, 500)	147.2	82.63	68.98	73.86	105.5	158.0	234.6	348.9
(14 km, 30, 1,000)	148.1	77.93	57.93	41.85	32.02	34.44	50.00	150.0
(14 km, 30, 1,500)	145.8	72.52	47.48	16.88	0.941	0.011	0.003	673.3
(14 km, 30, 2,000)	144.8	66.91	38.56	4.585	0	0	0.001	3593
(14 km, 50, 500)	419.4	231.8	194.2	210.0	313.7	526.0	942.7	1903
(14 km, 50, 1,000)	414.6	216.1	160.4	115.4	124.7	255.3	1453	2.6e4
(14 km, 50, 1,500)	410.1	199.9	127.7	41.58	14.17	22.19	3.0e4	6.9e4
(14 km, 50, 2,000)	404.0	183.9	97.26	7.364	0.050	1.5e4	61.e4	9.9e4
(14 km, 100, 500)	1156	659.4	585.4	803.1	2081	1.4e4	3.4e5	7.5e5
(14 km, 100, 1,000)	1145	626.2	513.2	759.5	4.8e4	6.5e5	1.1e6	1.5e6
(14 km, 100, 1,500)	1139	589.5	439.3	950.7	5.1e5	1.1e6	1.5e6	1.8e6
(14 km, 100, 2,000)	1130	553.5	372.2	6370	8.4e5	1.4e6	1.8e6	2.0e6

Note. The units are 10^{-14} m^3 s^{-1}.

Table C2
Results of Rate Coefficient $R_{A,a,0,q,100\%,500,5km}$

(A, q)	0.2 μm	0.4 μm	0.6 μm	1.0 μm	1.5 μm	2.0 μm	2.5 μm	3.0 μm
(3μm, 10e)	2.157	1.247	0.949	0.851	1.104	1.507	2.030	—
(3 μm, 20e)	3.421	2.130	1.621	1.306	1.384	1.740	2.255	—
(3 μm, 50e)	7.570	4.838	3.971	2.853	2.411	2.360	2.628	—
(3 μm, 100e)	14.40	9.284	10.96	5.572	4.487	3.962	3.789	—
(6 μm, 10e)	7.881	4.491	3.445	3.267	4.457	6.400	8.972	12.04
(6 μm, 20e)	13.15	7.833	5.942	4.433	4.890	6.633	9.107	12.12
(6 μm, 50e)	30.48	18.84	14.56	10.63	8.152	8.214	9.997	12.67
(6 μm, 100e)	59.28	37.38	29.20	21.87	17.04	13.91	13.22	14.60
(9 μm, 10e)	16.29	9.651	7.912	7.323	10.19	14.84	21.12	28.49
(9 μm, 20e)	27.97	16.85	13.06	9.668	11.00	15.31	21.25	28.53
(9 μm, 50e)	65.79	40.27	31.43	22.61	17.42	18.23	22.86	29.61
(9 μm, 100e)	129.8	81.59	62.98	46.86	36.37	29.51	29.02	33.39
(12 μm, 10e)	28.05	17.00	13.42	12.56	17.32	25.70	36.39	56.42
(12 μm, 20e)	48.05	29.39	22.25	16.20	18.93	26.18	36.75	50.79
(12 μm, 50e)	113.4	70.04	53.18	38.87	29.08	31.19	39.34	49.30
(12 μm, 100e)	226.1	140.0	107.2	80.20	60.50	49.12	48.80	49.04
(15 μm, 10e)	43.29	25.97	20.09	19.42	27.08	39.19	56.15	75.49
(15 μm, 20e)	73.93	44.88	33.73	25.27	29.11	40.19	56.85	75.71
(15 μm, 50e)	173.1	107.2	83.29	58.72	43.99	47.03	60.30	77.94
(15 μm, 100e)	348.8	216.3	169.8	122.9	91.36	72.36	73.67	86.11
(30 μm, 10e)	173.4	101.3	79.92	77.63	108.7	160.6	231.3	326.8
(30 μm, 20e)	295.6	177.3	133.6	99.09	116.2	163.7	233.2	328.2
(30 μm, 50e)	692.8	425.4	328.9	22.86	168.9	185.9	244.2	334.3
(30 μm, 100e)	1385	854.8	662.5	47.49	347.9	270.8	285.3	357.7
(50 μm, 10e)	448.4	265.3	209.0	211.0	317.3	516.2	858.3	1499
(50 μm, 20e)	760.2	463.6	349.9	262.8	333.1	522.9	862.8	1501
(50 μm, 50e)	1779	1108	851.5	594.4	453.1	572.2	889.4	1519
(50 μm, 100e)	3537	2220	1715	1235	910.4	759.1	984.5	1584
(100 μm, 10e)	829.1	518.0	432.2	585.4	1473	6866	1.6e5	4.2e5
(100 μm, 20e)	1415	905.6	700.7	665.4	1505	6896	1.6e5	4.2e5
(100 μm, 50e)	3307	2168	1702	1291	1730	7132	1.6e5	4.2e5
(100 μm, 100e)	6550	4313	3404	2674	2602	7950	1.6e5	4.2e5

Note. The units are 10^{-14} m^3 s^{-1}.

Table C3
Results of Rate Coefficient $R_{A,a,Q,0,100\%,1000,5km}$

(A, Q)	0.2 μm	0.4 μm	0.6 μm	1.0 μm	1.5 μm	2.0 μm	2.5 μm	3.0 μm
(3 μm, 0e)	1.157	0.690	0.603	0.547	0.534	0.492	0.380	—
(3 μm, 10e)	1.129	0.708	0.588	0.552	0.529	0.498	0.384	—
(3 μm, 20e)	1.147	0.717	0.603	0.552	0.543	0.515	0.409	—
(3 μm, 50e)	1.166	0.714	0.617	0.592	0.619	0.621	0.550	—
(3 μm, 100e)	1.190	0.736	0.629	0.710	0.883	1.051	1.100	—
(4 μm, 0e)	1.931	1.194	0.992	0.969	1.004	1.039	1.016	0.907
(4 μm, 10e)	1.935	1.199	1.024	0.966	1.004	1.034	1.025	0.902
(4 μm, 20e)	1.912	1.180	0.992	0.975	1.001	1.044	1.031	0.922
(4 μm, 50e)	1.920	1.185	1.031	0.991	1.041	1.102	1.116	1.027
(4 μm, 100e)	1.929	1.158	1.057	1.044	1.167	1.315	1.416	1.432
(5 μm, 0e)	2.918	1.804	1.503	1.490	1.612	1.773	1.898	1.922
(5 μm, 10e)	2.874	1.794	1.536	1.499	1.612	1.777	1.885	1.924
(5 μm, 20e)	2.881	1.794	1.441	1.503	1.625	1.779	1.907	1.944
(5 μm, 50e)	2.902	1.818	1.469	1.511	1.645	1.813	1.941	1.993
(5 μm, 100e)	2.928	1.814	1.545	1.543	1.708	1.923	2.123	2.222
(6 μm, 0e)	4.124	2.581	2.218	2.136	2.368	2.703	3.005	3.255

Table C3 *(continued)*

(A, Q)	0.2 μm	0.4 μm	0.6 μm	1.0 μm	1.5 μm	2.0 μm	2.5 μm	3.0 μm
(6 μm, 10e)	4.037	2.575	2.225	2.124	2.389	2.691	3.022	3.242
(6 μm, 20e)	4.103	2.560	2.251	2.147	2.355	2.691	3.015	3.261
(6 μm, 50e)	4.047	2.571	2.227	2.149	2.370	2.715	3.054	3.309
(6 μm, 100e)	4.068	2.589	2.231	2.182	2.428	2.790	3.149	3.459

Note. The units are 10^{-14} m^3 s^{-1}.

References

Beard, K. V., Ochs, H. T., & Twohy, C. H. (2004). Aircraft measurements of high average charges on cloud drops in layer clouds. *Geophysical Research Letters*, *31*, L14111. https://doi.org/10.1029/2004GL020465

Burns, G. B., Tinsley, B. A., French, W. J. R., Troshichev, O. A., & Frank-Kamenetsky, A. V. (2008). Atmospheric circuit influences on ground-level pressure in the Antarctic and Arctic. *Journal of Geophysical Research*, *113*, D15112. https://doi.org/10.1029/2007JD009618

COESA (1976). *U.S. Standard Atmosphere 1976, NOAA-S/T 76-1562*. Washington, DC: U.S. Govt. Printing Office.

Davenport, H. M., & Peters, L. K. (1978). Field studies of atmospheric particulate concentration changes during precipitation. *Atmospheric Environment*, *12*, 997–1008.

Davis, M. H. (1964a). *Two charged spherical conductors in a uniform electric field: Forces and field strength, RM-3860-PR* (p. 35). Santa Monica, Calif: The Rand Corp.

Davis, M. H. (1964b). Two charged spherical conductors in a uniform electric field: Forces and field strength. *Quarterly Journal of Mechanics and Applied Mathematics*, *17*, 400–511.

Feng, J. (2009). A size-resolved model for below-cloud scavenging of aerosols by snowfall. *Journal of Geophysical Research*, *114*, D08203. https://doi.org/10.1029/2008JD011012

Frank-Kamenetskii, A. V., Kotikov, A. L., Kruglov, A. A., Burns, G. B., Kleimenova, N. G., Kozyreva, O. V., et al. (2012). Variations in the near-surface atmospheric electric field at high latitudes and ionospheric potential during geomagnetic perturbations. *Geomagnetism and Aeronomy*, *52*(5), 629–638. https://doi.org/10.1134/S0016793212050064

Frederick, J. E. (2016). Solar irradiance observed at Summit, Greenland: Possible links to magnetic activity on short timescales. *Journal of Atmospheric and Solar - Terrestrial Physics*, *147*, 59–70. http://doi.org/10.1016/j.jastp.2016.07.001

Frederick, J. E. (2017). An analysis of couplings between solar activity and atmospheric opacity at the South Pole. *Journal of Atmospheric and Solar - Terrestrial Physics*, *164*, 97–104. http://doi.org/10.1016/j.jastp.2017.08.011

Frederick, J. E., & Tinsley, B. A. (2018). The response of longwave radiation at the South Pole to electrical and magnetic variations: Links to meteorological generators and the solar wind. *Journal of Atmospheric and Solar-Terrestrial Physics*, *179*, 214–224.

Hays, P. B., & Roble, R. G. (1979). A quasi-static model of global atmospheric electricity: I. The lower atmosphere. *Journal of Geophysical Research*, *84*, 3291–3305.

Humphries, R. S., Klekociuk, A. R., Schofield, R., Keywood, M., Ward, J., & Wilson, S. R. (2016). *Unexpectedly high ultrafine aerosol concentrations above East Antarctic sea ice*.

Khain, A., Arkhipov, V., Pinsky, M., Feldman, Y., & Ryabov, Y. (2004). Rain enhancement and fog elimination by seeding with charged droplets. Part I: Theory and numerical simulations. *Journal of Applied Meteorology*, *43*, 1513–1529.

Kniveton, D. R., Tinsley, B. A., Burns, G. B., Bering, E. A., & Troshichev, O. A. (2008). Variations in global cloud cover and the fair-weather vertical electric field. *Journal of Atmospheric and Solar-Terrestrial Physics*, *70*(13), 1633–1642.

Lam, M. M., Chisham, G., & Freeman, M. P. (2013). The interplanetary magnetic field influences mid-latitude surface atmospheric pressure. *Environmental Research Letters*, *8*, 045001. https://doi.org/10.1088/1748-9326/8/4/045001

Lam, M. M., Chisham, G., & Freeman, M. P. (2014). Solar-wind-driven geopotential height anomalies originate in the Antarctic lower troposphere. *Geophysical Research Letters*, *41*, 6509–6514. https://doi.org/10.1002/2014GL061421

Lam, M. M., Freeman, M. P., & Chisham, G. (2017). IMF-driven change to the Antarctic tropospheric temperature due to global atmospheric electric circuit. *Journal of Atmospheric and Solar - Terrestrial Physics*, *180*, 148–152. https://doi.org/10.1016/j.jastp.2017.08.027

Mauritsen, T., Sedlar, J., Tjernström, M., Leck, C., Martin, M., Shupe, M., Sjogren, S., et al. (2011). An Arctic CCN-limited cloud-aerosol regime. *Atmospheric Chemistry and Physics*, *11*(1), 165–173.

Nicoll, K. A., & Harrison, R. G. (2016). Stratiform cloud electrification: Comparison of theory with multiple in-cloud measurements. *Quarterly Journal of the Royal Meteorological Society*, *142*, 2679–2691. https://doi.org/10.1002/qj2858

Pruppacher, H. R., & Klett, J. D. (1997). *Microphysics of clouds and precipitation*, (2nd ed.p. 954). New York: Springer.

Rosenfeld, D., Kaufman, Y. K., & Koren, I. (2006). Switching cloud cover and dynamical regimes from open to closed Bernal cells in response to suppression of precipitation by aerosols. *Atmospheric Chemistry and Physics*, *6*, 2503–2511.

Rosenfeld, D., Lohmann, U., Raga, G. B., O'Dowd, C. D., Kulmala, M., Fuzzi, S., et al. (2008). Flood or drought: How do aerosols affect precipitation? *Science*, *321*(5894), 1309–1313. https://doi.org/10.1126/science.1160606

Shupe, M. D., Persson, P. O. G., Brooks, I. M., Tjernström, M., Sedlar, J., Mauritsen, T., et al. (2013). Cloud and boundary layer interactions over the Arctic sea-ice in late summer. *Atmospheric Chemistry and Physics*, *13*, 9379–9400. https://doi.org/10.5194/acp-13-9379-2013.

Silber, I., Verlinde, J., Eloranta, E. W., & Cadeddu, M. (2018). Antarctic Cloud Macrophysical, Thermodynamic Phase, and Atmospheric Inversion Coupling Properties at McMurdo Station: I. Principal Data Processing and Climatology. *Journal of Geophysical Research: Atmospheres*, *123*(11), 6099–6121.

Stone, R. S. (1993). Properties of austral winter clouds derived from radiometric profiles at the South Pole. *Journal of Geophysical Research Atmospheres*, *98*(D7), 12961–12971.

Tinsley, B. A. (2008). The global atmospheric electric circuit and its effects on cloud microphysics. *Reports on Progress in Physics*, *71*, 066801. (31 pp)

Tinsley, B. A. (2010). Electric charge modulation of aerosol scavenging in clouds: Rate coefficients with Monte Carlo simulation of diffusion. *Journal of Geophysical Research*, *115*, D23211. https://doi.org/10.1029/2010JD014580

Tinsley, B. A. (2012). A working hypothesis for connections between electrically-induced charges in cloud microphysics and storm vorticity, with possible effects on circulation. *Advances in Space Research*, *50*(2012), 791–805.

Tinsley, B. A., & Leddon, D. (2013). Charge modulation of scavenging in clouds: Extension of Monte-Carlo simulations and initial parameterization. *Journal of Geophysical Research: Atmospheres*, *118*, 8612–8624. https://doi.org/10.1002/jgrd.50618

Tinsley, B. A., Rohrbaugh, R. P., Hei, M., & Beard, K. V. (2000). Effects of image charges on the scavenging of aerosol particles by cloud droplets and on droplet charging and possible ice nucleation processes. *Journal of the Atmospheric Sciences*, *57*, 2118–2134.

Tinsley, B. A., & Zhou, L. (2006). Initial results of a global circuit model with stratospheric and tropospheric aerosols. *Journal of Geophysical Research*, *111*, D16205. https://doi.org/10.1029/2005JD006988

Tinsley, B. A., & Zhou, L. (2015). Parameterization of aerosol scavenging due to atmospheric ionization. *Journal of Geophysical Research: Atmospheres*, *120*, 8389–8410. https://doi.org/10.1002/2014JD023016

Tinsley, B. A., Zhou, L., & Plemmons, A. (2006). Changes in scavenging of particles by droplets due to weak electrification in clouds. *Atmospheric Research*, *79*, 266–295.

Twomey, B. (1977). The influence of pollution of the shortwave albedo of clouds. *Journal of the Atmospheric Sciences*, *34*, 1149–1152.

Wang, P. K., Grover, S. N., & Pruppacher, H. R. (1978). On the effect of electric charges on the scavenging of aerosol particles by clouds and small raindrops. *Journal of the Atmospheric Sciences*, *35*(9), 1735–1743.

Wang, P. K., & Ji, W. (2000). Collision efficiencies of ice crystals at low–intermediate Reynolds numbers colliding with supercooled cloud droplets: A numerical study. *Journal of the Atmospheric Sciences*, *57*(8), 1001–1009.

Williams, E. R. (2005). Lightning and climate: A review. *Atmospheric Research*, *76*, 272–287.

Young, K. C. (1993). *Microphysical processes in clouds* (p. 427). U.K.: Oxford Univ. Press.

Zhang, L., & Tinsley, B. A. (2018). Parameterization of in-cloud aerosol scavenging due to atmospheric ionization Part 2: Effects of varying particle density. *Journal of Geophysical Research: Atmospheres*, *123*, 3099–3115. https://doi.org/10.1002/2017JD027884

Zhang, L., Tinsley, B. A., & Zhou, L. (2018). Parameterization of in-cloud aerosol scavenging due to atmospheric ionization: Part 3. Effects of varying droplet radius. *Journal of Geophysical Research: Atmospheres*, *123*, 10,546–10,567. https://doi.org/10.1029/2018JD028840

Zhang, L., & Tinsley, B. A. (2017). Parameterization of aerosol scavenging due to atmospheric ionization under varying relative humidity. *Journal of Geophysical Research: Atmospheres*, *122*, 5330–5350. https://doi.org/10.1002/2016JD026255

Zhou, L., & Tinsley, B. A. (2007). Production of space charge at the boundaries of layer clouds. *Journal of Geophysical Research*, *112*, D11203. https://doi.org/10.1029/2006JD007998

Zhou, L., & Tinsley, B. A. (2012). Time dependent charging of layer clouds in the global electric circuit. *Advances in Space Research*, *50*, 828–842.

Zhou, L., Tinsley, B. A., & Plemmons, A. (2009). Scavenging in weakly electrified saturated and sub-saturated clouds, treating aerosol particles and droplets as conducting spheres. *Journal of Geophysical Research*, *114*, D18201. https://doi.org/10.1029/2008JD011527

Zhou, L., Tinsley, B. A., Wang, L., & Burns, G. (2017). The zonal-mean and regional tropospheric pressure responses to changes in ionospheric potential. *Journal of Atmospheric and Solar - Terrestrial Physics*, *171*, 111–118. https://doi.org/10.1016/j.jastp.2017.08.011